LITHOS 426-427 (2022) 106798

Contents lists available at ScienceDirect

LITHOS

journal homepage: www.elsevier.com/locate/lithos

# Petrogenesis of peridotites in the Dargai Complex ophiolite, Indus Suture Zone, Northern Pakistan: Implications for two stages of melting, depletion, and enrichment of the Neo-Tethyan mantle

Zaheen Ullah [a,b], Asad Khan [c], Shah Faisal [d], Tehseen Zafar [e,f], Huan Li [a,*], Muhammad Farhan [g]

[a] Key Laboratory of Metallogenic Prediction of Nonferrous Metals and Geological Environment Monitoring, Ministry of Education, School of Geosciences and Info-Physics, Central South University, Changsha 410083, China
[b] Department of Geosciences, University of Baltistan Skardu, Skardu 16100, Pakistan
[c] Department of Geology, FATA University, Tribal Subdivision Darra, Kohat 26100, KP, Pakistan
[d] National Centre of Excellence in Geology, University of Peshawar, Peshawar 25120, KP, Pakistan
[e] School of Earth and Space Science, Peking University, Beijing 100871, China
[f] State Key Laboratory of Ore Deposit Geochemistry, Institute of Geochemistry, Chinese Academy of Sciences, Guiyang 550081, China
[g] Marine Science Department, Zhejiang University, Zhoushan 316021, China

ARTICLE INFO

*Keywords:*
Upper mantle peridotites
Partial melting
Melt percolation and refertilization
*Re*-Os isotopic composition
Northern Pakistan

ABSTRACT

The upper mantle section of the Dargai ophiolite along the Indus Suture Zone, also known as the Main Mantle Thrust of northern Pakistan, consists mainly of clinopyroxene-bearing (Cpx)-harzburgites, depleted harzburgites, and dunites. Here we document a two-stage origin for these ultramafic rocks using new mineral and whole-rock geochemistry, integrated with *Re*-Os isotopic data of these upper mantle peridotites. Chromian spinel in the Cpx-harzburgites have significantly lower Cr# values (15.2–20.7) than the depleted harzburgites (38.4–75.2) and dunites (75.0–81.9). The Cpx-harzburgites are characterized by high average $Al_2O_3$ (2.04 wt%), CaO (2.26 wt%), ∑REE (24.3 ppb), and $^{187}Os/^{188}Os$ values ranging between 0.12495 and 0.12997. In contrast, the depleted harzburgites and dunites are characterized by lower average $Al_2O_3$ (0.51 wt% and 0.14 wt%, respectively), CaO (0.68 wt% and 0.19 wt%, respectively), and ∑REE (3.41 ppb and 0.92 ppb, respectively). The $^{187}Os/^{188}Os$ of the depleted harzburgites range between 0.11699 and 0.12612, values that are less radiogenic than those of the Cpx-harzburgites. The mantle-normalized trace element patterns of the Cpx-harzburgites reflect low degrees of partial melting (~10–15%), whereas those of the depleted harzburgites and dunites record somewhat higher degrees of partial melting (~15–23% additional melting of the Cpx-harzburgites). The low degree of melting, coupled with low degrees of melt extraction, therefore point to a spreading center at amid-ocean ridge (MOR) or in a distal forearc basin. In contrast, the depleted harzburgites and dunites formed during the second stage of melting and related refertilization, and were clearly linked to a supra-subduction zone (SSZ) setting. The *Re*-Os isotopic compositions of the Dargai Complex peridotites provide model ages of ca. 250 and ca. 450 Ma recording protracted tectonic events in close association with the geodynamic evolution of the Neo-Tethyan, Rheic, and Proto-Tethyan oceans. The extremely heterogeneous Os isotopic compositions of this part of the Neo-Tethyan upper mantle reflect multiple melt production and melt extraction processes throughout its tectonic evolution.

## 1. Introduction

Ophiolites generally represent relics of ancient oceanic lithosphere generated during seafloor spreading, and later tectonically emplaced onto continental margins or arc assemblages (Dilek and Furnes, 2011). Peridotites, interpreted as the solid residues of partial melting of the upper mantle, are major components of most ophiolites (Dilek and Furnes, 2014). Petrological and geochemical studies of ophiolitic abyssal and fore-arc peridotites have provided new insights into the upper mantle compositional variability, which has been primarily caused by differing degrees of partial melting (Dai et al., 2011; Dilek et al., 2007; Dilek and Thy, 2009; Morishita et al., 2011; Niu et al., 2013; Saccani and Tassinari, 2015; Shallo and Dilek, 2003; Uysal et al., 2015). The critical mineralogical and textural features of some peridotites are inconsistent

* Corresponding author.
*E-mail address:* lihuan@csu.edu.cn (H. Li).

https://doi.org/10.1016/j.lithos.2022.106798
Received 23 February 2022; Received in revised form 5 July 2022; Accepted 8 July 2022
Available online 16 July 2022

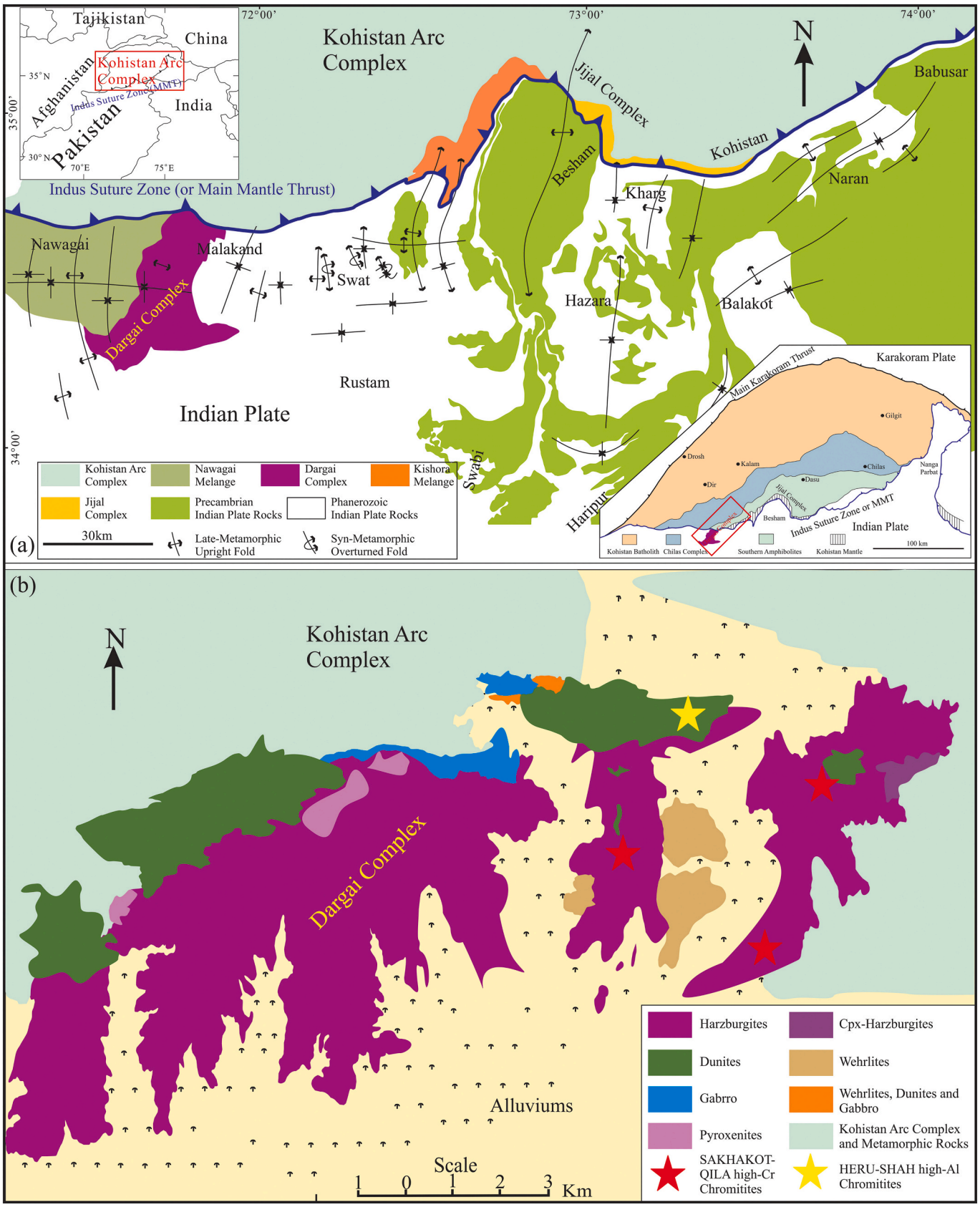


**Fig. 1.** (a) Simplified geological map of the Kohistan Arc Complex (KAC), Northern Pakistan, showing the location of the Dargai Complex (modified after Burg et al. (1998). The small inset map shows the location of the KAC in Northern Pakistan; (b) geological map of the Dargai Complex (modified after Ahmed, 1982, 1984), presenting different lithologies and some economical grade podiform chromitites (see discussion sections).

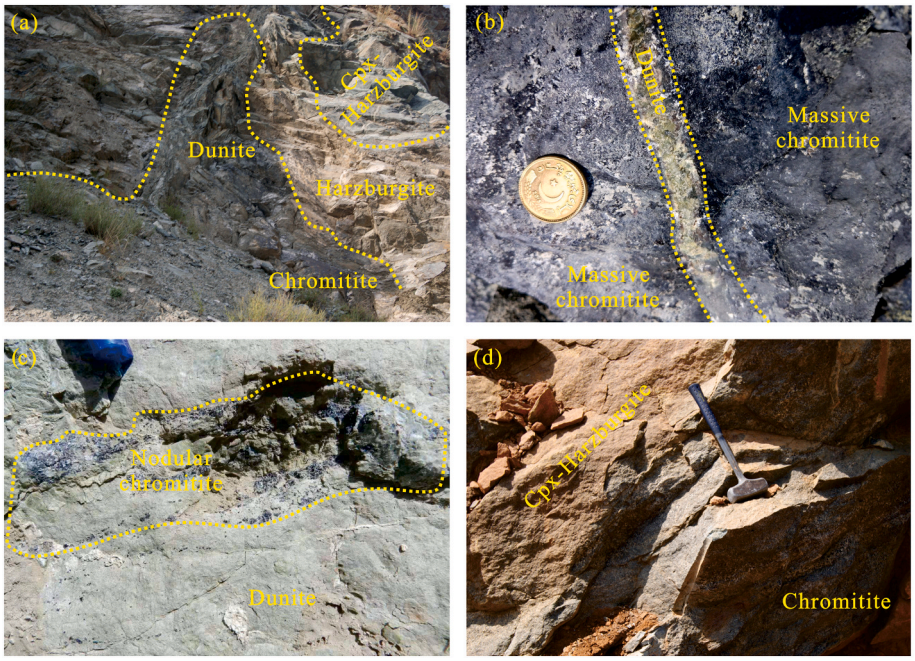


**Fig. 2.** Field photographs of the Dargai Complex peridotites and associated chromitites; (a) dunite and chromitite occurring as lenses or patches in fresh harzburgite; (b) massive chromitite body with a dunite vein; (c) lenses or patches of nodular chromitite with dunite; (d) massive chromitite band in Cpx-harzburgite.

with a simple residual origin and are thought to result from late-stage melt impregnation (Dilek and Furnes, 2014; Page and Barnes, 2009; Saccani et al., 2018). Therefore, mantle compositions reflect not only partial melting but also extensive melt-rock reaction (Dai et al., 2011; Dilek and Furnes, 2014; Morishita et al., 2011; Page and Barnes, 2009; Saccani et al., 2018; Zhou et al., 2005). Moreover, melt percolation and melt-rock reaction can cause significant variations in both platinum group elements (PGE) and *Re*-Os isotopic compositions (Barnes and Lightfoot, 2005; Batanova et al., 2008; Feng et al., 2018; Gao et al., 1999; Uysal et al., 2012; Xiong et al., 2017; Zhou et al., 2005). Mineral compositions in peridotites also document significant physical and chemical conditions in the upper mantle during their post-subsolidus evolution.

Studies of the structural, geochemical, and petrological features of ophiolitic mantle peridotites are by far the leading source of direct evidence on upper mantle compositions and structures. Much of the early research on ophiolites was focused on their crustal units but it is equally important to document the deformation and compositional features of the associated asthenospheric and lithospheric units (Kakar et al., 2014; Lian et al., 2018; Mahmood et al., 1995; Moghadam et al., 2013). The well-preserved and relatively fresh peridotites of the Dargai ophiolite, whose regional tectonic development has been well documented, are ideal natural laboratories to examine the chemical geodynamics of an ancient upper mantle.

A recent comprehensive investigation of a small massif of upper mantle peridotites in the Dargai Complex has illustrated its compositionally diverse characteristics, such as the existence of high-Al and high-Cr chromitites with varying chalcophile element abundances, including Ni, Cu, and PGE (Ullah et al., 2020a, 2020b). In this paper we present new detailed mineral chemistry, whole-rock (major, trace and PGE) geochemistry and *Re*-Os isotopic data for these ophiolitic peridotites to constrain their mantle melt evolution within the framework of the Tethyan tectonics of the Indus Suture Zone (ISZ). Our new data also provide a better understanding on the heterogeneous nature of the Neo-Tethyan mantle emplaced along this >2000-km-long suture zone.

## 2. Geological setting of the Dargai Complex ophiolite

Tethyan ophiolites i.e. Dongbo-Western Tibet China, Jijal Complex-Northern Pakistan, Waziristan-Northwest Pakistan, Muslim Bagh-West Pakistan, Semail-Oman, Troodos-Cyprus, and Kizildag-Turkey etc., are oceanic lithosphere remnants, as well as some SSZ accumulations which were formed during the closure of the Tethyan ocean and collision of the Gondwana and Eurasian continents (Dilek et al., 2007; Dilek and Furnes, 2018; Kakar et al., 2014; Mahmood et al., 1995; Ullah et al., 2020a, 2020b; Xiong et al., 2015). The Main Karakoram Thrust (MKT) marks the boundary between the Karakoram block and the Kohistan Arc Complex (KAC) in the north, whereas the ISZ or Main Mantle Thrust (MMT) separates the KAC form the Indian plate farther south (Fig. 1a). The KAC, which was formed during intra-oceanic subduction of the Neo-Tethyan lithosphere and later docked on the Karakoram plate, separates the continental masses of the Indian and Karakoram blocks, (Burg et al., 1998; Schaltegger et al., 2002). To the northwest, the Indian Plate is in tectonic contact with the southeastern part of the Afghan Plate (Fig. 1a). Both the ISZ and the western collisional zone with the Afghan Plate contain several mafic-ultramafic (ophiolitic) complexes that originated within the Neo-Tethyan Ocean (Arif and Jan, 2006; Dipietro et al., 2000; Kakar et al., 2014; Ullah et al., 2020a; Ullah et al., 2020b).

A mafic-ultramafic mélange that occurs along the ISZ is known as the Dargai Complex (Fig. 1a), which has been interpreted as a part of a south-directed thrust fault on the Indian Plate that was active during the Late Cretaceous (Schaltegger et al., 2002). The Dargai Complex (also called the Harichand Ophiolitic Complex (Ahmed, 1982; Ahmed, 1984; Arif and Jan, 2006; Ullah et al., 2020a; Ullah et al., 2020b), mainly consists of a southerly arcuate, ultramafic complex that extends NNE-SSW for ~30 km, with an average width of 3 to 6 km. The complex was obducted onto metamorphosed pelites, and other carbonaceous and calcareous rocks that range in age from Precambrian to Triassic (Ahmed, 1984). Blueschist facies metamorphism took place in Early/Late Cretaceous as indicated by $^{40}$Ar-$^{39}$Ar phengite ages of 85–99 Ma and thus, records a pre-collisional metamorphism within the Indus Suture Zone (Dipietro et al., 2000). The compositional and textural variations of chromitites and associated phases in the Dargai Complex have been studied in some detail by Ahmed (1982, 1984) and Ullah et al. (2020b).

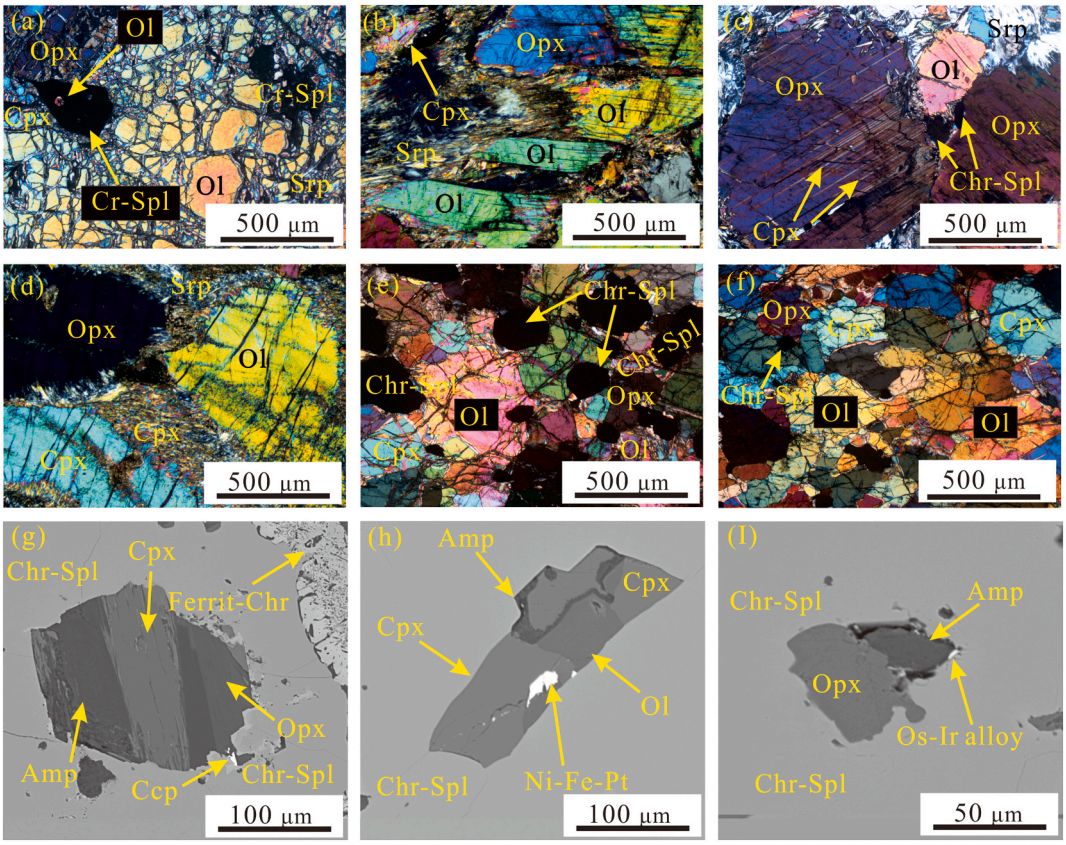


**Fig. 3.** Photomicrographs illustrating petrological and mineralogical features of the peridotites and chromitites of the Dargai Complex ophiolite; (a) fractured olivine have contacts with grains of orthopyroxene, clinopyroxene, and Cr-spinel; (b) elongate olivine crystals in Cpx-harzburgite that are partly altered (cross-polarized light); (c) large orthopyroxene grain with Cpx lamellae accompanied by smaller olivine grains (cross-polarized light) in depleted harzburgite; (d) large olivine and orthopyroxene crystals surrounded by small grains of clinopyroxene; (e) coarse-grained olivine, orthopyroxene and Cr-spinel in a fresh sample of dunite (cross-polarized light); (f) grain boundary migration caused extensive fracture of olivine, orthopyroxene and clinopyroxene in coarse-grained dunite; (g) relatively large grain of chromite in dunite showing marginal alteration to ferrit-chromitite and containing a polymineralic inclusion containing orthopyroxene, clinopyroxene, amphibole, and chalcopyrite; (h) elongate, polymineralic inclusion in chromite containing olivine, clinopyroxene, amphibole and a small alloy of Ni-Fe-Pt minerals in chromite of a Cpx-harzburgite; (i) polymineralic inclusion in chromite composed of olivine orthopyroxene, from containing occur in the chromian spinels of harzburgite which amphibole, orthopyroxene, clinopyroxene, and an Os-Ir alloy. Abbreviations: Ol: Olivine, Cpx: clinopyroxene, Opx: orthopyroxene, Cr-spl: chromian spinel, Srp: serpentine, Ferrit-Chr: ferrit chromite, Amp: amphibole and Ccp: chalcopyrite.

The chromitites in the Dargai Complex crop out in two horizons; one in the southern (lower or Sakhakot-Qila) zone has Cr# values >60, the second in a northern (upper or Heru-Shah) zone that has Cr# values <60 (Fig. 1b). The high-Cr chromitites are thought to have formed in a SSZ setting, whereas the high-Al chromitites were most likely crystallized in a Mid-Ocean Ridge (MOR) or possibly in a back arc environment (Ballhaus, 1998; Dilek et al., 2007; Khedr et al., 2014; Robinson et al., 1997; Ullah et al., 2020a; Ullah et al., 2020b; Uysal et al., 2012; Zhou et al., 1998). The ultramafic rocks of the Dargai ophiolites (Fig. 1a) are composed of 65% harzburgite, 23% dunite (which increases to the northward), 8% wehrlite, and 4% chromitite and sparse dikes including pyroxenites and serpentinites (Fig. 1b). The pyroxenite dikes are composed chiefly of clinopyroxene, but a few also have small amounts of orthopyroxene and are classified as websterite (Ahmed, 1982, 1984).

From the top to bottom (also from north to south) of the ISZ, the ophiolite is composed of Cpx-harzburgite and depleted harzburgite (Fig. 2a), and numerous bodies of chromitite (Fig. 2b–d) that are associated with a 400- to 600-m-thick zone of dunite (Fig. 1b). The dunite corresponds to the mantle-crust transition zone (MTZ) (Ahmed, 1982, 1984; Arif and Jan, 2006; Jan and Howie, 1981; Ullah et al., 2020a, 2020b). There is a sharp contact between the MTZ dunites and harzburgites, which has been interpreted to be the petrologic-MOHO. The crustal section of the Dargai ophiolite, which is generally 1 to 2 km thick, crops out discontinuously along the western margin of the ophiolite where it consists mainly of gabbros and pyroxenites. The lowest part of the mafic crustal unit consists of interlayered wehrlites and dunites of MTZ (Fig. 1b).

## 3. Petrographic features of the Dargai peridotites

The Cpx-harzburgites of the Dargai Complex are mainly comprised of 66–78 vol% olivine, 17–28 vol% orthopyroxene, 4–5 vol% clinopyroxene, and < 2 vol% Cr-spinel. These rocks are characterized by granular textures (Fig. 3a) and show weak banding or layering (Fig. 3b), which has been partially overprinted by massive hydrothermal alteration. Serpentine and chlorite occur along cracks and grain boundaries of olivine leaving small relict enclaves (Fig. 3a and b). Cr-spinel grains are scattered along the banding of the Cpx-harzburgites (Fig. 3a), where they contain abundant solid, polymineralic inclusions of amphibole, clinopyroxene, minor olivine, some base metal sulfides (Cpx-harzburgites: chalcopyrite, millerite and pentlandite), and minor nickel-iron-platinum alloys (Fig. 3h), all of which range in size from 5 to 100 μm.

The Dargai depleted harzburgites mostly consist of olivine (70 to 84 vol%), orthopyroxene (14 to 24 vol%), and clinopyroxene (1 to 5 vol%) along with minor Cr-spinel (Fig. 3c). Generally, the textures are porphyroblastic with large crystals of olivine and orthopyroxene that show evidence of plastic deformation with such features as kink banding,

**Table 1**
Representative compositions of olivine in the Dargai Complex peridotites determined by EPMA (wt%).

| Lithology | S. No | $SiO_2$ | $Al_2O_3$ | $TiO_2$ | $Cr_2O_3$ | FeO | MnO | MgO | CaO | NiO | $Na_2O$ | $K_2O$ | Total | Fo |
|---|---|---|---|---|---|---|---|---|---|---|---|---|---|---|
| **Cpx-Harzburgite** | Cpx-H-1 | 40.48 | 0.01 | 0.01 | 0.01 | 9.53 | 0.13 | 49.69 | 0.05 | 0.39 | 0.02 | 0.00 | 100.32 | 90.3 |
| | Cpx-H-2 | 40.50 | 0.03 | 0.00 | 0.03 | 9.77 | 0.16 | 50.13 | 0.01 | 0.41 | 0.00 | 0.01 | 101.05 | 90.1 |
| | Cpx-H-3 | 40.61 | 0.01 | 0.02 | 0.00 | 9.45 | 0.18 | 50.09 | 0.03 | 0.38 | 0.01 | 0.01 | 100.79 | 90.4 |
| | Cpx-H-4 | 40.43 | 0.00 | 0.03 | 0.02 | 9.69 | 0.12 | 49.81 | 0.02 | 0.42 | 0.00 | 0.00 | 100.54 | 90.2 |
| | Cpx-H-5 | 40.48 | 0.02 | 0.01 | 0.01 | 9.33 | 0.15 | 49.46 | 0.02 | 0.40 | 0.00 | 0.01 | 99.89 | 90.4 |
| | Cpx-H-6 | 40.65 | 0.01 | 0.02 | 0.00 | 9.99 | 0.17 | 49.43 | 0.04 | 0.41 | 0.01 | 0.00 | 100.73 | 89.8 |
| | Cpx-H-7 | 40.57 | 0.01 | 0.01 | 0.03 | 9.85 | 0.15 | 49.79 | 0.03 | 0.42 | 0.00 | 0.01 | 100.87 | 90.0 |
| | Cpx-H-8 | 39.91 | 0.00 | 0.03 | 0.02 | 9.36 | 0.18 | 49.62 | 0.01 | 0.38 | 0.01 | 0.00 | 99.52 | 90.4 |
| | Cpx-H-9 | 39.98 | 0.03 | 0.01 | 0.01 | 9.96 | 0.17 | 49.58 | 0.03 | 0.41 | 0.01 | 0.00 | 100.19 | 89.9 |
| | Cpx-H-10 | 40.19 | 0.02 | 0.00 | 0.01 | 9.66 | 0.13 | 50.05 | 0.02 | 0.39 | 0.00 | 0.01 | 100.48 | 90.2 |
| **Harzburgite** | Hrz-1 | 40.72 | 0.02 | 0.02 | 0.05 | 8.53 | 0.13 | 50.97 | 0.01 | 0.38 | 0.01 | 0.00 | 100.84 | 91.4 |
| | Hrz-2 | 40.28 | 0.01 | 0.02 | 0.01 | 8.81 | 0.11 | 51.12 | 0.01 | 0.35 | 0.00 | 0.01 | 100.73 | 91.2 |
| | Hrz-3 | 40.49 | 0.01 | 0.01 | 0.03 | 8.29 | 0.14 | 50.43 | 0.02 | 0.39 | 0.01 | 0.00 | 99.82 | 91.6 |
| | Hrz-4 | 40.69 | 0.02 | 0.02 | 0.05 | 8.47 | 0.13 | 51.33 | 0.02 | 0.42 | 0.00 | 0.01 | 101.16 | 91.5 |
| | Hrz-5 | 40.43 | 0.02 | 0.02 | 0.02 | 8.59 | 0.13 | 50.62 | 0.02 | 0.45 | 0.00 | 0.01 | 100.31 | 91.3 |
| | Hrz-6 | 40.19 | 0.01 | 0.02 | 0.01 | 8.74 | 0.12 | 50.39 | 0.01 | 0.38 | 0.00 | 0.00 | 99.87 | 91.1 |
| | Hrz-7 | 40.11 | 0.01 | 0.01 | 0.03 | 8.44 | 0.11 | 50.12 | 0.03 | 0.41 | 0.01 | 0.01 | 99.29 | 91.4 |
| | Hrz-8 | 40.57 | 0.01 | 0.01 | 0.04 | 8.69 | 0.14 | 50.57 | 0.01 | 0.44 | 0.00 | 0.01 | 100.49 | 91.2 |
| | Hrz-9 | 40.33 | 0.02 | 0.02 | 0.02 | 8.99 | 0.12 | 50.81 | 0.01 | 0.43 | 0.02 | 0.00 | 100.77 | 91.0 |
| | Hrz-10 | 40.65 | 0.02 | 0.02 | 0.05 | 8.88 | 0.13 | 50.45 | 0.03 | 0.42 | 0.01 | 0.01 | 100.67 | 91.0 |
| **Dunite** | Dn-1 | 40.69 | 0.01 | 0.02 | 0.02 | 7.77 | 0.10 | 51.52 | 0.06 | 0.44 | 0.00 | 0.00 | 100.63 | 92.2 |
| | Dn-2 | 41.18 | 0.01 | 0.01 | 0.02 | 7.13 | 0.11 | 51.39 | 0.04 | 0.43 | 0.00 | 0.01 | 100.33 | 92.8 |
| | Dn-3 | 41.37 | 0.00 | 0.00 | 0.01 | 7.44 | 0.11 | 51.13 | 0.03 | 0.41 | 0.01 | 0.01 | 100.52 | 92.5 |
| | Dn-4 | 40.74 | 0.04 | 0.01 | 0.02 | 7.21 | 0.12 | 51.48 | 0.05 | 0.43 | 0.02 | 0.00 | 100.12 | 92.7 |
| | Dn-5 | 40.71 | 0.02 | 0.02 | 0.00 | 7.71 | 0.13 | 51.41 | 0.03 | 0.44 | 0.01 | 0.01 | 100.49 | 92.2 |
| | Dn-6 | 40.91 | 0.02 | 0.00 | 0.01 | 7.54 | 0.10 | 51.44 | 0.06 | 0.42 | 0.00 | 0.01 | 100.51 | 92.4 |
| | Dn-7 | 41.32 | 0.03 | 0.00 | 0.01 | 7.11 | 0.12 | 51.25 | 0.04 | 0.44 | 0.01 | 0.01 | 100.34 | 92.8 |
| | Dn-8 | 40.61 | 0.02 | 0.01 | 0.02 | 7.14 | 0.13 | 51.32 | 0.05 | 0.43 | 0.00 | 0.00 | 99.73 | 92.8 |
| | Dn-9 | 40.65 | 0.01 | 0.01 | 0.02 | 7.29 | 0.11 | 51.38 | 0.03 | 0.41 | 0.02 | 0.00 | 99.93 | 92.6 |
| | Dn-10 | 40.87 | 0.04 | 0.02 | 0.00 | 7.51 | 0.12 | 51.29 | 0.03 | 0.42 | 0.00 | 0.01 | 100.31 | 92.4 |

*Note*: Oxide values in weight percent; forsterite, Fo = 100 Mg/(Mg + $Fe^{2+}$).

rotation, and recrystallization. Cr-spinel occurs along the rims of orthopyroxene crystals or as small, euhedral crystals in olivine or between the major phases (Fig. 3c). Some of the orthopyroxene grains contain clinopyroxene exsolution lamellae (Fig. 3c) and show deformational features including elongations and kink bands (Fig. 3c). Some irregular interstitial clinopyroxene is also sandwiched between the large

**Table 2**
Representative compositions of orthopyroxene in the Dargai Complex peridotites determined by EPMA (wt%).

| Lithology | S. No | $SiO_2$ | $Al_2O_3$ | $TiO_2$ | $Cr_2O_3$ | FeO | MnO | MgO | CaO | NiO | $Na_2O$ | $K_2O$ | En | Fs | Wo | Mg# |
|---|---|---|---|---|---|---|---|---|---|---|---|---|---|---|---|---|
| **Cpx-Harzburgite** | Cpx-H-1 | 53.44 | 4.53 | 0.05 | 0.61 | 6.28 | 0.14 | 33.02 | 1.25 | 0.1 | 0.05 | 0.01 | 88.2 | 9.41 | 2.40 | 90.4 |
| | Cpx-H-2 | 53.91 | 3.91 | 0.07 | 0.68 | 6.55 | 0.14 | 32.86 | 1.55 | 0.09 | 0.02 | 0.04 | 87.3 | 9.76 | 2.96 | 89.9 |
| | Cpx-H-3 | 54.12 | 5.12 | 0.06 | 0.72 | 6.13 | 0.14 | 32.45 | 0.75 | 0.1 | 0.01 | 0.03 | 89.1 | 9.44 | 1.48 | 90.4 |
| | Cpx-H-4 | 54.25 | 4.28 | 0.05 | 0.55 | 6.22 | 0.15 | 32.77 | 1.61 | 0.1 | 0.03 | 0.03 | 87.6 | 9.33 | 3.09 | 90.4 |
| | Cpx-H-5 | 53.71 | 3.99 | 0.04 | 0.59 | 6.54 | 0.16 | 31.95 | 1.71 | 0.1 | 0.01 | 0.02 | 86.7 | 9.96 | 3.34 | 89.7 |
| | Cpx-H-6 | 54.09 | 4.68 | 0.08 | 0.64 | 6.29 | 0.14 | 33.02 | 1.23 | 0.09 | 0.02 | 0.03 | 88.2 | 9.43 | 2.36 | 90.4 |
| | Cpx-H-7 | 53.51 | 5.08 | 0.06 | 0.71 | 6.12 | 0.15 | 32.98 | 0.93 | 0.09 | 0.05 | 0.01 | 88.9 | 9.26 | 1.80 | 90.6 |
| | Cpx-H-8 | 53.67 | 4.33 | 0.05 | 0.66 | 6.39 | 0.14 | 32.16 | 0.99 | 0.09 | 0.04 | 0.04 | 88.2 | 9.83 | 1.95 | 89.9 |
| | Cpx-H-9 | 53.89 | 4.58 | 0.04 | 0.62 | 6.11 | 0.16 | 32.64 | 1.62 | 0.1 | 0.02 | 0.01 | 87.7 | 9.21 | 3.13 | 90.5 |
| | Cpx-H-10 | 54.16 | 4.79 | 0.06 | 0.68 | 6.32 | 0.14 | 32.39 | 1.54 | 0.1 | 0.03 | 0.02 | 87.4 | 9.57 | 2.99 | 90.1 |
| **Harzburgite** | Hrz-1 | 55.94 | 2.16 | 0.03 | 0.65 | 5.85 | 0.12 | 33.91 | 0.79 | 0.10 | 0.01 | 0.03 | 89.8 | 8.69 | 1.50 | 91.2 |
| | Hrz-2 | 56.69 | 2.09 | 0.02 | 0.45 | 5.58 | 0.14 | 34.99 | 0.84 | 0.06 | 0.02 | 0.02 | 90.4 | 8.08 | 1.56 | 91.8 |
| | Hrz-3 | 55.87 | 1.81 | 0.02 | 0.51 | 5.52 | 0.13 | 34.75 | 1.18 | 0.08 | 0 | 0.01 | 89.8 | 8.01 | 2.19 | 91.8 |
| | Hrz-4 | 56.71 | 1.43 | 0.01 | 0.62 | 5.67 | 0.13 | 34.84 | 1.01 | 0.07 | 0.02 | 0.01 | 89.9 | 8.21 | 1.87 | 91.6 |
| | Hrz-5 | 56.14 | 2.02 | 0.03 | 0.49 | 5.74 | 0.12 | 35.12 | 0.96 | 0.06 | 0.01 | 0.02 | 89.9 | 8.25 | 1.77 | 91.6 |
| | Hrz-6 | 56.13 | 1.97 | 0.01 | 0.55 | 5.55 | 0.13 | 34.64 | 0.99 | 0.09 | 0.01 | 0.01 | 90.1 | 8.09 | 1.85 | 91.8 |
| | Hrz-7 | 56.27 | 1.11 | 0.02 | 0.63 | 5.79 | 0.15 | 34.57 | 1.12 | 0.12 | 0.02 | 0.03 | 89.5 | 8.41 | 2.08 | 91.4 |
| | Hrz-8 | 56.52 | 1.95 | 0.01 | 0.59 | 5.72 | 0.15 | 34.45 | 1.08 | 0.11 | 0 | 0 | 89.6 | 8.35 | 2.02 | 91.5 |
| | Hrz-9 | 55.93 | 1.77 | 0.03 | 0.48 | 5.57 | 0.12 | 35.08 | 1.11 | 0.08 | 0 | 0 | 89.9 | 8.01 | 2.05 | 91.8 |
| | Hrz-10 | 56.36 | 1.79 | 0.02 | 0.54 | 5.62 | 0.13 | 33.68 | 1.05 | 0.12 | 0.02 | 0.01 | 89.6 | 8.39 | 2.01 | 91.4 |
| **Dunite** | Dn-1 | 56.33 | 0.84 | 0.01 | 0.38 | 5.34 | 0.11 | 34.48 | 1.36 | 0.06 | 0.02 | 0 | 89.7 | 7.79 | 2.54 | 92.0 |
| | Dn-2 | 56.28 | 0.79 | 0.01 | 0.26 | 5.26 | 0.13 | 34.71 | 1.08 | 0.08 | 0.01 | 0 | 90.3 | 7.68 | 2.02 | 92.2 |
| | Dn-3 | 56.21 | 0.51 | 0 | 0.31 | 5.11 | 0.11 | 34.74 | 1.19 | 0.13 | 0 | 0.01 | 90.3 | 7.45 | 2.22 | 92.4 |
| | Dn-4 | 56.45 | 0.75 | 0.02 | 0.42 | 4.98 | 0.12 | 33.95 | 1.58 | 0.14 | 0 | 0.01 | 89.6 | 7.38 | 2.99 | 92.4 |
| | Dn-5 | 56.33 | 0.98 | 0 | 0.35 | 5.41 | 0.13 | 34.71 | 0.67 | 0.13 | 0.02 | 0.01 | 90.8 | 7.94 | 1.26 | 91.9 |
| | Dn-6 | 56.44 | 0.56 | 0 | 0.45 | 5.09 | 0.11 | 33.99 | 1.53 | 0.11 | 0.02 | 0 | 89.6 | 7.51 | 2.90 | 92.3 |
| | Dn-7 | 56.42 | 0.95 | 0.01 | 0.37 | 4.99 | 0.12 | 34.41 | 0.65 | 0.14 | 0 | 0.01 | 91.3 | 7.43 | 1.24 | 92.5 |
| | Dn-8 | 56.53 | 0.66 | 0.01 | 0.29 | 5.55 | 0.11 | 34.89 | 0.87 | 0.09 | 0.01 | 0.01 | 90.3 | 8.06 | 1.62 | 91.8 |
| | Dn-9 | 56.27 | 0.71 | 0.02 | 0.38 | 5.37 | 0.13 | 34.58 | 0.99 | 0.08 | 0.02 | 0 | 90.3 | 7.86 | 1.86 | 91.9 |
| | Dn-10 | 56.48 | 0.96 | 0.01 | 0.43 | 5.48 | 0.13 | 34.43 | 1.45 | 0.11 | 0.01 | 0.01 | 89.3 | 7.98 | 2.70 | 91.8 |

*Note:* Values in weight percent. Chemical formulae calculated on the basis of 6 oxygens; wollastonite, Wo = 100 Ca/(Ca + Mg + $Fe^{2+}$); enstatite, En = 100 Mg/(Ca + Mg + $Fe^{2+}$); ferrosilite, Fs = 100 $Fe^{2+}$/(Ca + Mg + $Fe^{2+}$); Mg# = 100 Mg/(Mg + $Fe^{2+}$).

**Table 3**
Representative compositions of clinopyroxene in the Dargai Complex peridotites determined by EPMA (wt%).

| Lithology | S. No | $SiO_2$ | $Al_2O_3$ | $TiO_2$ | $Cr_2O_3$ | FeO | MnO | MgO | CaO | NiO | $Na_2O$ | $K_2O$ | En | Fs | Wo | Mg# |
|---|---|---|---|---|---|---|---|---|---|---|---|---|---|---|---|---|
| | Cpx-H-1 | 50.75 | 3.97 | 0.19 | 0.79 | 2.37 | 0.07 | 17.22 | 23.08 | 0.04 | 0.23 | 0 | 49.0 | 3.78 | 47.2 | 92.8 |
| | Cpx-H-2 | 50.75 | 4.49 | 0.15 | 0.94 | 2.26 | 0.09 | 16.65 | 23.11 | 0.03 | 0.29 | 0.01 | 48.2 | 3.67 | 48.1 | 92.9 |
| | Cpx-H-3 | 49.21 | 4.78 | 0.21 | 1.02 | 2.29 | 0.08 | 16.88 | 23.02 | 0.03 | 0.51 | 0 | 48.6 | 3.70 | 47.7 | 92.9 |
| | Cpx-H-4 | 51.34 | 3.65 | 0.17 | 0.88 | 2.31 | 0.07 | 16.52 | 22.99 | 0.05 | 0.45 | 0.01 | 48.1 | 3.77 | 48.1 | 92.7 |
| | Cpx-H-5 | 51.44 | 5.19 | 0.24 | 1.07 | 2.36 | 0.09 | 16.02 | 23.14 | 0.05 | 0.25 | 0.02 | 47.2 | 3.89 | 48.9 | 92.4 |
| | Cpx-H-6 | 50.26 | 4.72 | 0.22 | 0.96 | 2.39 | 0.08 | 16.31 | 23.23 | 0.04 | 0.48 | 0.01 | 47.5 | 3.90 | 48.6 | 92.4 |
| | Cpx-H-7 | 49.55 | 5.58 | 0.23 | 1.09 | 2.38 | 0.07 | 17.11 | 22.98 | 0.05 | 0.54 | 0.01 | 48.9 | 3.82 | 47.2 | 92.8 |
| | Cpx-H-8 | 51.16 | 3.89 | 0.17 | 0.99 | 2.38 | 0.09 | 17.29 | 23.06 | 0.03 | 0.36 | 0 | 49.1 | 3.79 | 47.1 | 92.8 |
| | Cpx-H-9 | 51.26 | 5.09 | 0.21 | 0.82 | 2.26 | 0.09 | 16.36 | 22.98 | 0.05 | 0.28 | 0 | 47.9 | 3.71 | 48.4 | 92.8 |
| **Cpx-Harzburgite** | Cpx-H-10 | 50.63 | 4.53 | 0.15 | 0.86 | 2.29 | 0.08 | 16.84 | 23.19 | 0.04 | 0.31 | 0.02 | 48.4 | 3.69 | 47.9 | 92.9 |
| | Hrz-1 | 53.12 | 1.58 | 0.04 | 0.39 | 1.71 | 0.06 | 17.22 | 24.51 | 0.02 | 0.14 | 0.01 | 48.1 | 2.68 | 49.2 | 94.7 |
| | Hrz-2 | 52.94 | 2.26 | 0.03 | 0.45 | 1.99 | 0.08 | 17.59 | 23.98 | 0.01 | 0.04 | 0.01 | 48.9 | 3.11 | 47.9 | 94.0 |
| | Hrz-3 | 53.47 | 3.29 | 0.07 | 0.41 | 1.79 | 0.06 | 17.26 | 24.55 | 0.06 | 0.08 | 0.01 | 48.1 | 2.79 | 49.1 | 94.5 |
| | Hrz-4 | 51.44 | 3.15 | 0.05 | 0.78 | 1.97 | 0.09 | 19.15 | 23.39 | 0.04 | 0.09 | 0 | 51.7 | 2.98 | 45.4 | 94.5 |
| | Hrz-5 | 53.38 | 1.08 | 0.07 | 0.91 | 1.76 | 0.08 | 18.98 | 23.91 | 0.02 | 0.08 | 0.01 | 51.1 | 2.66 | 46.3 | 95.1 |
| | Hrz-6 | 53.16 | 2.51 | 0.02 | 0.83 | 1.97 | 0.09 | 18.31 | 24.26 | 0.01 | 0.03 | 0.01 | 49.7 | 2.99 | 47.3 | 94.3 |
| | Hrz-7 | 52.66 | 1.98 | 0.03 | 0.55 | 1.83 | 0.07 | 18.18 | 23.72 | 0.06 | 0.11 | 0 | 50.2 | 2.83 | 47.0 | 94.7 |
| | Hrz-8 | 51.91 | 3.07 | 0.05 | 1.18 | 1.85 | 0.06 | 18.89 | 23.47 | 0.03 | 0.09 | 0 | 51.3 | 2.82 | 45.8 | 94.8 |
| | Hrz-9 | 51.76 | 2.35 | 0.07 | 1.07 | 1.71 | 0.08 | 19.17 | 24.21 | 0.05 | 0.08 | 0.01 | 51.1 | 2.56 | 46.4 | 95.2 |
| **Harzburgite** | Hrz-10 | 52.59 | 2.77 | 0.02 | 0.98 | 1.77 | 0.09 | 19.01 | 24.06 | 0.03 | 0.12 | 0.01 | 50.9 | 2.66 | 46.4 | 95.0 |
| | Dn-1 | 54.12 | 0.78 | 0.02 | 0.51 | 1.44 | 0.08 | 19.57 | 23.19 | 0.14 | 0.09 | 0 | 52.8 | 2.18 | 44.9 | 96.0 |
| | Dn-2 | 53.24 | 1.39 | 0.01 | 0.18 | 1.67 | 0.07 | 19.91 | 23.48 | 0.11 | 0.07 | 0.02 | 52.8 | 2.48 | 44.7 | 95.5 |
| | Dn-3 | 54.49 | 0.59 | 0.05 | 0.72 | 1.63 | 0.06 | 17.77 | 23.43 | 0.05 | 0.09 | 0.02 | 50.0 | 2.57 | 47.4 | 95.1 |
| | Dn-4 | 53.94 | 1.16 | 0.05 | 0.38 | 1.52 | 0.05 | 20.08 | 23.12 | 0.08 | 0.02 | 0 | 53.5 | 2.27 | 44.3 | 95.9 |
| | Dn-5 | 53.99 | 0.51 | 0.02 | 0.25 | 1.71 | 0.08 | 18.79 | 23.28 | 0.06 | 0.09 | 0.01 | 51.5 | 2.62 | 45.9 | 95.1 |
| | Dn-6 | 53.31 | 0.93 | 0.03 | 0.77 | 1.49 | 0.05 | 20.34 | 23.24 | 0.09 | 0.04 | 0 | 53.7 | 2.21 | 44.1 | 96.0 |
| | Dn-7 | 54.35 | 1.11 | 0.02 | 0.33 | 1.79 | 0.06 | 18.84 | 23.61 | 0.07 | 0.04 | 0 | 51.2 | 2.73 | 46.1 | 94.9 |
| | Dn-8 | 54.28 | 0.98 | 0.02 | 0.56 | 1.51 | 0.08 | 18.23 | 23.64 | 0.12 | 0.08 | 0.01 | 50.6 | 2.35 | 47.1 | 95.6 |
| | Dn-9 | 54.21 | 0.77 | 0.05 | 0.52 | 1.45 | 0.05 | 19.99 | 23.14 | 0.09 | 0.06 | 0.02 | 53.4 | 2.17 | 44.4 | 96.1 |
| **Dunite** | Dn-10 | 53.69 | 1.26 | 0.01 | 0.64 | 1.75 | 0.07 | 17.96 | 23.65 | 0.11 | 0.02 | 0.01 | 49.9 | 2.73 | 47.3 | 94.8 |

*Note*: Values in weight percent. Chemical formulae calculated on the basis of 6 oxygens. Wollastonite, Wo = 100 Ca/(Ca + Mg + $Fe^{2+}$); enstatite, En = 100 Mg/(Ca + Mg + $Fe^{2+}$); ferrosilite, Fs = 100 $Fe^{2+}$ /(Ca + Mg + $Fe^{2+}$); Mg# = 100 Mg/(Mg + $Fe^{2+}$).

olivine and orthopyroxene grains (Fig. 3d). Residual Cr-spinel in the depleted harzburgites occurs as small, brown to reddish-brown, interstitial grains, mostly along the rims of olivine crystals. The depleted harzburgites are mainly fresh with only sparse cracks filled by serpentine and chlorite. Exsolution lamellae and kink banding in the harzburgites suggest that these rocks originated under high-strain

**Table 4**
Representative compositions of spinel in the Dargai Complex peridotites determined by EPMA (wt%).

| Lithology | S. No | $SiO_2$ | $Al_2O_3$ | $TiO_2$ | $Cr_2O_3$ | FeO | MnO | MgO | CaO | NiO | $Na_2O$ | $K_2O$ | Total | Mg# | Cr# |
|---|---|---|---|---|---|---|---|---|---|---|---|---|---|---|---|
| | Cpx-H-1 | 0.11 | 51.85 | 0.05 | 17.86 | 13.01 | 0.10 | 18.38 | 0.02 | 0.27 | 0.01 | 0.01 | 101.7 | 72.6 | 18.8 |
| | Cpx-H-2 | 0.08 | 53.19 | 0.06 | 15.23 | 12.89 | 0.12 | 17.22 | 0.02 | 0.30 | 0.01 | 0.03 | 99.15 | 71.3 | 16.1 |
| | Cpx-H-3 | 0.12 | 53.94 | 0.04 | 14.43 | 12.55 | 0.13 | 17.87 | 0.01 | 0.28 | 0.01 | 0.01 | 99.39 | 72.8 | 15.2 |
| | Cpx-H-4 | 0.07 | 53.44 | 0.05 | 16.44 | 13.42 | 0.12 | 17.67 | 0.01 | 0.31 | 0.09 | 0.01 | 101.6 | 71.1 | 17.1 |
| | Cpx-H-5 | 0.09 | 48.14 | 0.06 | 18.45 | 14.59 | 0.13 | 18.09 | 0.01 | 0.28 | 0.05 | 0.02 | 99.91 | 69.8 | 20.5 |
| | Cpx-H-6 | 0.10 | 53.77 | 0.04 | 15.94 | 13.04 | 0.12 | 17.99 | 0.01 | 0.28 | 0.01 | 0.01 | 101.3 | 71.9 | 16.6 |
| | Cpx-H-7 | 0.12 | 52.59 | 0.06 | 15.78 | 13.45 | 0.11 | 18.95 | 0.01 | 0.30 | 0.01 | 0.00 | 101.4 | 72.5 | 16.8 |
| | Cpx-H-8 | 0.06 | 53.95 | 0.05 | 15.98 | 12.37 | 0.11 | 18.91 | 0.02 | 0.31 | 0.02 | 0.00 | 101.8 | 73.8 | 16.6 |
| | Cpx-H-9 | 0.10 | 48.33 | 0.04 | 18.85 | 15.28 | 0.13 | 18.71 | 0.02 | 0.29 | 0.01 | 0.01 | 101.8 | 69.4 | 20.7 |
| **Cpx-Harzburgite** | Cpx-H-10 | 0.08 | 52.68 | 0.06 | 16.53 | 14.15 | 0.11 | 18.42 | 0.01 | 0.30 | 0.03 | 0.00 | 102.4 | 70.6 | 17.4 |
| | Hrz-1 | 0.07 | 19.45 | 0.03 | 48.76 | 17.12 | 0.16 | 13.73 | 0.02 | 0.05 | 0.00 | 0.01 | 99.40 | 59.4 | 62.7 |
| | Hrz-2 | 0.02 | 11.95 | 0.07 | 54.11 | 23.03 | 0.35 | 11.44 | 0.02 | 0.07 | 0.00 | 0.01 | 101.1 | 47.2 | 75.2 |
| | Hrz-3 | 0.05 | 36.81 | 0.04 | 34.17 | 15.80 | 0.21 | 13.51 | 0.01 | 0.14 | 0.02 | 0.00 | 100.8 | 60.9 | 38.4 |
| | Hrz-4 | 0.13 | 26.99 | 0.07 | 44.69 | 19.72 | 0.15 | 8.94 | 0.02 | 0.09 | 0.00 | 0.00 | 100.8 | 45.6 | 52.6 |
| | Hrz-5 | 0.11 | 12.79 | 0.05 | 56.51 | 20.29 | 0.15 | 11.44 | 0.01 | 0.11 | 0.02 | 0.01 | 101.5 | 50.9 | 74.8 |
| | Hrz-6 | 0.05 | 29.74 | 0.03 | 42.73 | 17.02 | 0.21 | 11.66 | 0.02 | 0.09 | 0.00 | 0.01 | 101.6 | 55.4 | 49.1 |
| | Hrz-7 | 0.10 | 25.41 | 0.05 | 42.99 | 16.33 | 0.26 | 15.31 | 0.02 | 0.11 | 0.01 | 0.00 | 100.6 | 63.4 | 53.2 |
| | Hrz-8 | 0.07 | 26.33 | 0.05 | 41.63 | 19.02 | 0.20 | 13.03 | 0.01 | 0.08 | 0.00 | 0.00 | 100.4 | 55.5 | 51.5 |
| | Hrz-9 | 0.05 | 24.55 | 0.07 | 43.84 | 17.87 | 0.21 | 14.02 | 0.01 | 0.07 | 0.02 | 0.01 | 100.7 | 58.8 | 54.5 |
| **Harzburgite** | Hrz-10 | 0.02 | 27.81 | 0.04 | 42.15 | 17.84 | 0.16 | 11.62 | 0.02 | 0.05 | 0.01 | 0.01 | 99.73 | 53.9 | 50.4 |
| | Dn-1 | 0.06 | 9.98 | 0.11 | 54.49 | 24.34 | 0.19 | 9.13 | 0.02 | 0.08 | 0.06 | 0.00 | 98.46 | 40.6 | 78.6 |
| | Dn-2 | 0.08 | 12.11 | 0.06 | 54.24 | 23.91 | 0.25 | 9.01 | 0.01 | 0.05 | 0.04 | 0.00 | 99.76 | 40.7 | 75.0 |
| | Dn-3 | 0.11 | 8.22 | 0.09 | 55.45 | 23.98 | 0.18 | 9.93 | 0.01 | 0.05 | 0.05 | 0.00 | 98.07 | 43.2 | 81.9 |
| | Dn-4 | 0.09 | 8.45 | 0.10 | 54.43 | 26.13 | 0.21 | 9.11 | 0.02 | 0.07 | 0.02 | 0.01 | 98.64 | 38.9 | 81.2 |
| | Dn-5 | 0.14 | 11.06 | 0.11 | 54.41 | 22.94 | 0.24 | 9.09 | 0.02 | 0.08 | 0.04 | 0.01 | 98.14 | 42.3 | 76.8 |
| | Dn-6 | 0.06 | 9.56 | 0.07 | 54.29 | 24.77 | 0.22 | 9.12 | 0.01 | 0.07 | 0.05 | 0.01 | 98.23 | 40.1 | 79.2 |
| | Dn-7 | 0.11 | 9.99 | 0.09 | 55.51 | 22.79 | 0.18 | 9.71 | 0.02 | 0.08 | 0.02 | 0.00 | 98.50 | 43.9 | 78.9 |
| | Dn-8 | 0.08 | 10.77 | 0.10 | 54.69 | 26.18 | 0.21 | 8.71 | 0.02 | 0.06 | 0.02 | 0.00 | 100.8 | 37.7 | 77.3 |
| | Dn-9 | 0.07 | 9.96 | 0.08 | 54.76 | 24.94 | 0.19 | 8.16 | 0.01 | 0.05 | 0.06 | 0.01 | 98.29 | 37.4 | 78.7 |
| **Dunite** | Dn-10 | 0.09 | 11.66 | 0.09 | 55.01 | 23.32 | 0.23 | 8.89 | 0.01 | 0.08 | 0.04 | 0.00 | 99.42 | 41.1 | 75.9 |

*Note:* Values in weight percent. Mg# = 100*Mg/(Mg + $Fe^{2+}$); Cr# = 100*Cr/(Cr + Al).

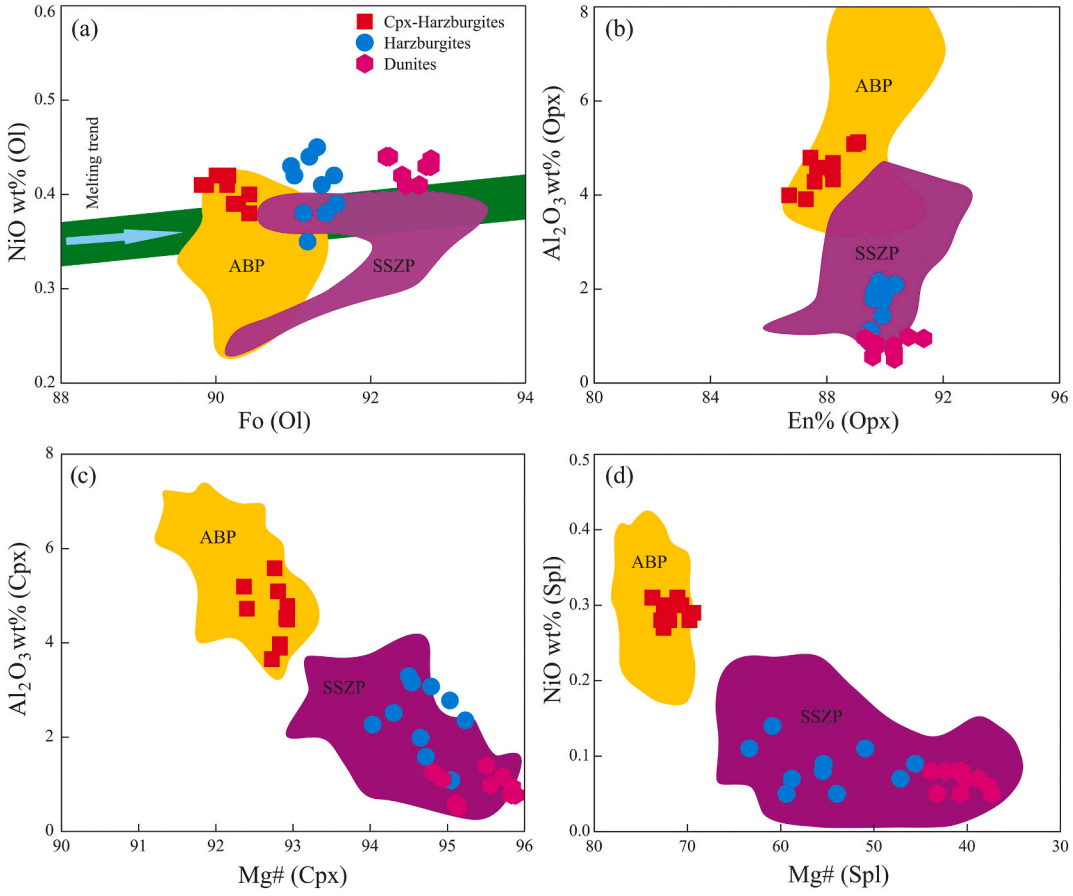


**Fig. 4.** Olivine, orthopyroxene, clinopyroxene and Cr-spinel compositional variations from the Dargai peridotite and dunite; (a) olivine (Fo versus NiO wt%); (b) orthopyroxene (En % versus $Al_2O_3$ wt%); (c) clinopyroxene (Mg# versus $Al_2O_3$ wt%); (d) Cr-spinel (NiO wt% versus Mg#). ABP (abyssal peridotite) and SSZP (supra-subduction zone peridotite) fields are from Ullah et al. (2020a) and Uysal et al. (2012). The partial melting trends and mantle olivine array are from Saka et al. (2014) and Wu et al. (2018). Fo and Mg# = 100 Mg/(Mg + $Fe^{2+}$); En = 100 Mg/ (Ca + Mg + $Fe^{2+}$).

conditions. Cr-spinel in the Dargai depleted peridotites makes up 1–2 vol % of most rocks. The platinum-group minerals (PGM), such as Os-Ir alloys are mostly associated with inclusions of amphibole and orthopyroxene in Cr-spinel grains within the depleted harzburgites (Fig. 3i).

Dunites common form narrow channels or lenses within the depleted harzburgites and consist almost entirely of granular olivine (92 to 96 vol %) with minor Cpx, Opx, and Cr-spinel (Fig. 3c). The olivine grains range in size from 0.5 to 1 mm and display wavy extinction and deformational twinning. However, some larger grains are intensively fractured (Fig. 3e). In contrast, clinopyroxene occurs as small, euhedral grains ranging in size from 0.3 to 0.5 mm. The Cr-spinel crystals, 0.2 to 0.5 mm in size, are generally dispersed as inclusions in the olivine, but locally their concentrations are high enough to form disseminated chromitites (Fig. 3f). These disseminated ore bodies range in thickness from 1 to 10 m and generally form lenticular to rod-like bodies (Fig. 2c and d) with nodular and massive textures, that are commonly enclosed by dunite envelopes (Fig. 2b). Cr-spinels in the dunites are typically euhedral or subhedral (Fig. 3e), apparently the result of interaction between percolating basaltic magma and the peridotite tectonites (Matsumoto and Arai, 2001). In the dunite samples, the Ch-spinel grains are altered to ferrite chromite on their margins and along cracks (Fig. 3g). Olivine grains in contact with the Cr-spinel are replaced by serpentine with bands of chlorite along the rims (Fig. 3c).

## 4. Methods and analytical procedures

Thirty fresh peridotite samples were collected, including 10 samples of Cpx-harzburgite from Heru-Shah, 10 samples of depleted harzburgite and 10 samples of dunite from the Sakhakot-Qila area of the Dargai Complex. Silicate minerals and associated Cr-spinels were analyzed for major elements using a JEOL JXA-8100 electron probe micro analyzer (EPMA) equipped with four wavelength-dispersive spectrometers (WDS) at the State Key Laboratory of Geological Processes and Mineral Resources, China University of Geosciences (Wuhan). The analyzing parameters of the EPMA were set at an accelerating voltage of 15 kV, a beam current of 20 nA and beam diameter of 1 μm. Natural and synthetic oxides and metals (eskolaite, Cr, Ni) were used as standards for non-silicates, whereas natural minerals were used for all silicates: (sanidine: K, pyrope: Al, almandine: Fe, diopside: Ca, jadeite: Na, rhodonite: Mn, forsterite: Si, Mg, and rutile: Ti) standards were used to calibrate the precision of the instrument. The $Fe^{3+}$ contents in chromite were calculated assuming an ideal chromian spinel stoichiometry of $A^{2+}B_2^{3+}O_4$. Representative compositions of the silicate minerals and chromian spinels are given in Tables 1–4.

Trace element concentrations of clinopyroxene grains in the Cpx-harzburgites and depleted harzburgites were obtained by laser ablation inductively coupled plasma-mass spectrometry (LA-ICPMS) at the Sample Solution Laboratory, Wuhan, China. The analyses were carried out on polished thick sections (>80 mm) using a 100 mJ pulse energy and 5 Hz rate of pulse repetition. The ablated materials were discharged in a continuous argon flow into the torch of an ELAN 6100 DRC ICP-MS using the certified reference material NIST SRM610 and $^{43}Ca$ as internal standards to correct for linear drift. Precision and accuracy (<10% and < 5%, respectively) were assessed on the USGS BCR-2 g reference glass.

Whole-rock trace elements were analyzed by a jana plasma quant inductively coupled plasma-mass spectrometer (ICP-MS) at the Institute

**Table 5**
Trace and REE element compositions (ppm) of selected clinopyroxenes in the Dargai Complex peridotites.

| Rocks | Cpx-Harzburgite | | | | | | | | | | Harzburgite | | | | | | | | | |
|---|---|---|---|---|---|---|---|---|---|---|---|---|---|---|---|---|---|---|---|---|
| S. No | Cpx-H-1 | Cpx-H-2 | Cpx-H-3 | Cpx-H-4 | Cpx-H-5 | Cpx-H-6 | Cpx-H-7 | Cpx-H-8 | Cpx-H-9 | Cpx-H-10 | H-1 | H-2 | H-3 | H-4 | H-5 | H-6 | H-7 | H-8 | H-9 | H-10 |
| **Sc** | 57.38 | 59.01 | 53.27 | 41.61 | 56.84 | 55.41 | 49.29 | 45.16 | 51.68 | 54.33 | 50.6 | 55.46 | 46.18 | 49.34 | 50.0 | 52.91 | 44.82 | 52.13 | 53.54 | 54.73 |
| **V** | 216 | 236 | 211 | 302 | 246 | 251 | 231 | 279 | 242 | 198 | 187 | 235 | 151 | 226 | 157 | 197 | 146 | 205 | 184 | 205 |
| **Cr** | 8941 | 6085 | 3868 | 7899 | 2946 | 8544 | 7438 | 5571 | 4212 | 4528 | 7255 | 6132 | 7709 | 3512 | 6228 | 8155 | 9391 | 8861 | 4813 | 9149 |
| **Co** | 31.99 | 19.62 | 18.73 | 26.88 | 20.89 | 24.41 | 16.56 | 21.39 | 18.08 | 28.56 | 17.09 | 19.97 | 22.58 | 18.91 | 23.96 | 18.34 | 23.16 | 17.82 | 20 | 22 |
| **Ni** | 351 | 396 | 274 | 291 | 307 | 284 | 349 | 269 | 318 | 328 | 337 | 287 | 319 | 355 | 299 | 288 | 309 | 365 | 315 | 334 |
| **Zn** | 13.85 | 8.95 | 7.68 | 4.19 | 10.16 | 5.83 | 11.77 | 7.36 | 5.99 | 9.41 | 12.25 | 8.27 | 5.94 | 11.07 | 5.99 | 13.62 | 6.77 | 10.53 | 7.44 | 10.16 |
| **Rb** | 0.521 | 1.991 | 0.035 | 0.180 | 0.174 | 0.050 | 0.127 | 0.048 | 0.394 | 0.152 | 0.071 | 0.103 | 0.119 | 0.053 | 0.088 | 0.038 | 0.057 | 0.074 | 0.046 | 0.077 |
| **Sr** | 0.563 | 0.299 | 0.116 | 0.776 | 0.485 | 0.098 | 0.369 | 0.419 | 0.025 | 0.322 | 0.327 | 0.108 | 0.589 | 0.256 | 0.419 | 0.501 | 0.029 | 0.544 | 0.216 | 0.059 |
| **Y** | 8.455 | 7.551 | 6.631 | 4.444 | 8.828 | 4.848 | 9.222 | 6.115 | 8.194 | 7.099 | 3.863 | 4.118 | 0.397 | 3.542 | 4.266 | 0.903 | 1.728 | 0.578 | 0.822 | 2.187 |
| **Zr** | 0.395 | 0.322 | 0.856 | 0.442 | 0.269 | 0.095 | 0.023 | 0.801 | 0.561 | 0.388 | 0.027 | 0.089 | 0.019 | 0.161 | 0.093 | 0.071 | 0.082 | 0.041 | 0.036 | 0.045 |
| **Nb** | 0.001 | 0.000 | 0.025 | 0.007 | 0.033 | 0.002 | 0.018 | 0.000 | 0.015 | 0.029 | 0.027 | 0.039 | 0.000 | 0.000 | 0.025 | 0.011 | 0.009 | 0.011 | 0.021 | 0.007 |
| **Cs** | 0.029 | 0.008 | 0.224 | 0.011 | 0.028 | 0.030 | 0.016 | 0.011 | 0.015 | 0.004 | 0.099 | 0.058 | 0.145 | 0.006 | 0.111 | 0.008 | 0.047 | 0.020 | 0.003 | 0.033 |
| **Ba** | 0.039 | 1.540 | 0.437 | 0.097 | 0.066 | 0.853 | 0.091 | 0.114 | 0.135 | 0.422 | 0.094 | 0.047 | 0.328 | 0.031 | 0.055 | 0.588 | 0.289 | 0.129 | 0.067 | 0.040 |
| **La** | 0.008 | 0.119 | 0.015 | 0.018 | 0.004 | 0.012 | 0.006 | 0 | 0.027 | 0.005 | 0.016 | 0.351 | 0.077 | 0.008 | 0.029 | 0.011 | 0.004 | 0.049 | 0.013 | 0.021 |
| **Ce** | 0.022 | 0.027 | 0.015 | 0.125 | 0.069 | 0.084 | 0.133 | 0.004 | 0.067 | 0.079 | 0.062 | 0.013 | 0.355 | 0.016 | 0.046 | 0.008 | 0.010 | 0.094 | 0.018 | 0.157 |
| **Pr** | 0.016 | 0.011 | 0.025 | 0.023 | 0.004 | 0.018 | 0.031 | 0.042 | 0.033 | 0.008 | 0.068 | 0.042 | 0.003 | 0.072 | 0.056 | 0.003 | 0.085 | 0.019 | 0.008 | 0.029 |
| **Nd** | 0.112 | 0.253 | 0.024 | 0.166 | 0.098 | 0.209 | 0.184 | 0.139 | 0.355 | 0.195 | 0.029 | 0.031 | 0.047 | 0.059 | 0.038 | 0.027 | 0.051 | 0.024 | 0.035 | 0.029 |
| **Sm** | 0.199 | 0.385 | 0.264 | 0.133 | 0.076 | 0.216 | 0.025 | 0.287 | 0.171 | 0.323 | 0.064 | 0.056 | 0.037 | 0.051 | 0.021 | 0.033 | 0.048 | 0.028 | 0.061 | 0.053 |
| **Eu** | 0.099 | 0.138 | 0.126 | 0.021 | 0.112 | 0.176 | 0.044 | 0.195 | 0.149 | 0.074 | 0.028 | 0.031 | 0.016 | 0.026 | 0.039 | 0.026 | 0.021 | 0.034 | 0.023 | 0.037 |
| **Gd** | 0.209 | 0.681 | 0.533 | 0.748 | 0.816 | 0.799 | 0.956 | 0.444 | 0.824 | 0.909 | 0.189 | 0.042 | 0.079 | 0.204 | 0.174 | 0.093 | 0.163 | 0.027 | 0.118 | 0.028 |
| **Tb** | 0.199 | 0.151 | 0.221 | 0.183 | 0.098 | 0.069 | 0.129 | 0.146 | 0.204 | 0.218 | 0.048 | 0.038 | 0.067 | 0.071 | 0.061 | 0.025 | 0.034 | 0.042 | 0.011 | 0.059 |
| **Dy** | 0.971 | 1.544 | 1.724 | 1.916 | 1.613 | 1.435 | 0.641 | 1.822 | 1.299 | 1.118 | 0.555 | 0.491 | 0.862 | 0.628 | 0.875 | 0.069 | 0.019 | 0.468 | 0.035 | 0.584 |
| **Ho** | 0.335 | 0.441 | 0.256 | 0.219 | 0.177 | 0.398 | 0.405 | 0.359 | 0.282 | 0.313 | 0.039 | 0.116 | 0.012 | 0.097 | 0.137 | 0.058 | 0.029 | 0.161 | 0.141 | 0.022 |
| **Er** | 1.222 | 0.853 | 1.257 | 0.441 | 1.303 | 0.999 | 1.346 | 0.721 | 0.574 | 1.196 | 0.484 | 0.117 | 0.585 | 0.418 | 0.077 | 0.208 | 0.526 | 0.096 | 0.374 | 0.189 |
| **Tm** | 0.173 | 0.098 | 0.196 | 0.133 | 0.184 | 0.061 | 0.144 | 0.099 | 0.116 | 0.128 | 0.096 | 0.021 | 0.029 | 0.053 | 0.109 | 0.074 | 0.014 | 0.101 | 0.079 | 0.039 |
| **Yb** | 0.678 | 1.146 | 1.235 | 1.206 | 1.189 | 0.713 | 0.479 | 0.845 | 1.099 | 0.954 | 0.643 | 0.159 | 0.476 | 0.094 | 0.108 | 0.671 | 0.298 | 0.515 | 0.494 | 0.128 |
| **Lu** | 0.155 | 0.126 | 0.172 | 0.054 | 0.139 | 0.084 | 0.112 | 0.186 | 0.101 | 0.093 | 0.029 | 0.101 | 0.063 | 0.047 | 0.056 | 0.036 | 0.088 | 0.014 | 0.025 | 0.095 |
| **Hf** | 0.112 | 0.086 | 0.139 | 0.097 | 0.022 | 0.209 | 0.162 | 0.195 | 0.259 | 0.049 | 0.019 | 0.027 | 0.025 | 0.022 | 0.034 | 0.025 | 0.032 | 0.029 | 0.027 | 0.031 |
| **Ta** | 0.001 | 0.003 | 0.004 | 0.000 | 0.000 | 0.005 | 0.006 | 0.003 | 0.000 | 0.000 | 0.006 | 0 | 0.004 | 0.013 | 0 | 0.009 | 0.007 | 0.004 | 0.005 | 0.008 |
| **Pb** | 0.239 | 0.512 | 0.187 | 0.491 | 0.827 | 0.279 | 0.049 | 0.603 | 0.099 | 0.333 | 0.297 | 0.411 | 0.036 | 2.581 | 0.074 | 4.779 | 0.901 | 1.922 | 3.428 | 0.861 |
| **Th** | 0.005 | 0.000 | 0.003 | 0.000 | 0.007 | 0.004 | 0.000 | 0.000 | 0.006 | 0.003 | 0.000 | 0.005 | 0.000 | 0.003 | 0.000 | 0.004 | 0.006 | 0.003 | 0.000 | 0.004 |
| **U** | 0.007 | 0.000 | 0.003 | 0.005 | 0.007 | 0.000 | 0.009 | 0.003 | 0.000 | 0.004 | 0.000 | 0.002 | 0.01 | 0.000 | 0.01 | 0.00 | 0.00 | 0.01 | 0.01 | 0.01 |
| **Ti** | 1083 | 1295 | 1016 | 1199 | 709 | 1102 | 839 | 971 | 764 | 911 | 126 | 248 | 92 | 411 | 424 | 338 | 489 | 299 | 202 | 475 |

*Note*: Cpx = clinopyroxene; REE = rare earth elements.

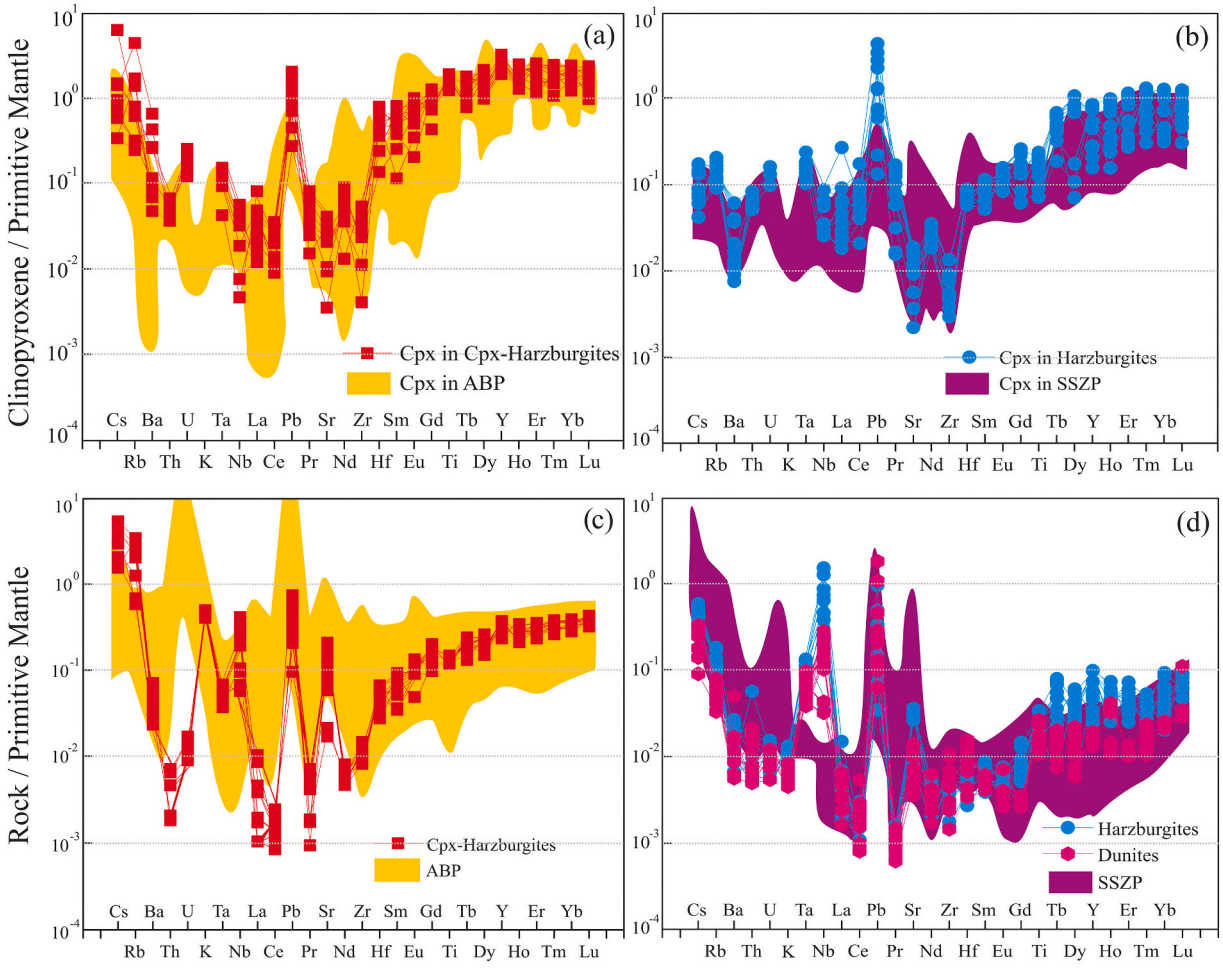


**Fig. 5.** Primitive mantle-normalized trace element spider diagrams for representative clinopyroxene grains in Cpx-harzburgite samples (a), depleted harzburgite samples (b), whole-rock analyses for Cpx-harzburgite samples (c) and depleted harzburgite and dunite samples (d) from the Dargai peridotites and dunite. Normalizing values are from Palme and O'Neill (2013). Abyssal peridotite field is from Niu et al. (1997) and the forearc peridotite field is from Parkinson and Pearce (1998).

of Geochemistry, Chinese Academy of Sciences, using the technique of Liang et al. (2000). About 0.05 g of specimen powder was put in a PTFE, and 3 ml of $HNO_3$ and 0.6 ml of HF were added and then heated to 185°C in an electric oven for about 24 h. The bombs were evaporated to dryness after cooling. Five hundred ng of Rh was then added as an internal standard, followed by 4 ml of water and 3 ml of $HNO_3$. The bomb was resealed and heated again to 135°C for 5 h to dissolve any impurities. After cooling, the final dilution factor for ICP-MS results was about 3000. The analytical precision was generally better than ~5% for elements with concentrations >10 ppm, and 10% for those with concentrations <10 ppm.

The sample preparation method for the major elements was the same as for the trace elements and the dilution factor for the measurement of elements by ICP-OES (Inductively coupled plasma-optical emission spectrometry) (Agilent 720) was approximately 1000. For $SiO_2$ measurements, standard gravimetric procedures were utilized. For LOI determinations about 1 g of sample powder was heated in a muffle furnace to 900°C for about 1 h, and utilizing the weights before and after heating. The accuracies of the ICP-OES analyses are estimated to be ±5% (relative) for the concentrations of minor oxides between 0.1 wt% and 0.5 wt% and ± 2% (relative) for concentrations of major oxides >0.5%. The analytical results and uncertainties of reference materials OU-6 (Slate) and AMH-1 (Andesite) agree well with published values (Potts and Kane, 2005; Thompson et al., 2000). The ICP-MS analytical consistencies are expected to be greater than ±5–10% (relative) for most elements.

The PGE concentrations of the peridotites were measured using the Jackson et al. (1990) nickel sulfide fire assay and Te-coprecipitation technique, followed by ICP-MS analysis. A standard sample (GBW079290) was used as a PGE reference to determine the accuracy of the analyses (Sun and Sun, 2005). The consistencies of the analysis were better than 5% for Ir, Rh, and Pd, and 10% for Os, Ru, Pt. The detection limits for PGEs and results of representative analyses are given in Table 7.

The *Re*-Os isotope compositions of the peridotites were investigated in the Re-Os isotope Key Laboratory, Chinese Academy of Geological Sciences, Beijing. Approximately 0.5–0.6 g of finely powdered samples were precisely weighed and placed into Carius tubes together with $^{185}Re$-$^{190}Os$ spikes and digested with reverse aqua regia (6 mL of concentrated $HNO_3$ and 2 mL of concentrated HCL), and heated in an oven for about 24 h at 230°C. The rhenium fraction was separated and purified using acetone in an 8 mol/L NaOH solution, and Osmium was separated by solvent extraction into $CCl_4$ and back-extracted into concentrated HBr followed by clean-up via microdistillation. A detailed description of this procedure is available in Li et al. (2015; 2014). The isotopic compositions and Re and Os abundances were measured by negative-thermal ionization mass spectrometry (N-TIMS; Thermo-Finnigan Triton) in electron multiplier mode at CAGS, Beijing (Li et al., 2014; Li et al., 2015). The reported $^{192}Os/^{188}Os$ ratios were normalized to 3.08271 to correct for instrumented mass fractionation of

**Table 6**
Major and trace elements compositions of whole-rock samples in the Dargai Complex peridotites.

| Rocks | Cpx-Harzburgite | | | | | | | | | | Harzburgite | | | | | | | | | | Dunite | | | | | | | | | |
|---|---|---|---|---|---|---|---|---|---|---|---|---|---|---|---|---|---|---|---|---|---|---|---|---|---|---|---|---|---|---|
| S. No | Cpx-H-1 | Cpx-H-2 | Cpx-H-3 | Cpx-H-4 | Cpx-H-5 | Cpx-H-6 | Cpx-H-7 | Cpx-H-8 | Cpx-H-9 | Cpx-H-10 | H-1 | H-2 | H-3 | H-4 | H-5 | H-6 | H-7 | H-8 | H-9 | H-10 | D-1 | D-2 | D-3 | D-4 | D-5 | D-6 | D-7 | D-8 | D-9 | D-10 |
| **$SiO_2$** | 45.16 | 44.22 | 45.49 | 44.49 | 44.91 | 43.94 | 44.12 | 44.71 | 44.26 | 44.59 | 44.88 | 43.37 | 44.42 | 43.23 | 43.55 | 42.98 | 44.23 | 43.74 | 44.16 | 43.91 | 39.91 | 40.53 | 40.12 | 39.99 | 40.32 | 40.69 | 40.49 | 40.64 | 39.44 | 40.26 |
| **$TiO_2$** | 0.029 | 0.026 | 0.031 | 0.034 | 0.032 | 0.039 | 0.016 | 0.028 | 0.024 | 0.031 | 0.002 | 0.006 | 0.003 | 0.008 | 0.002 | 0.002 | 0.001 | 0.001 | 0.004 | 0.003 | 0.004 | 0.001 | 0.002 | 0.002 | 0.001 | 0.001 | 0.001 | 0.003 | 0.001 | 0.002 |
| **$Al_2O_3$** | 2.15 | 2.11 | 1.98 | 1.79 | 2.02 | 2.08 | 1.85 | 2.21 | 2.24 | 1.96 | 0.55 | 0.66 | 0.71 | 0.81 | 0.42 | 0.64 | 0.48 | 0.31 | 0.18 | 0.34 | 0.11 | 0.18 | 0.06 | 0.13 | 0.08 | 0.22 | 0.11 | 0.16 | 0.14 | 0.19 |
| **$Fe_2O_3$** | 9.05 | 8.91 | 9.16 | 8.95 | 9.11 | 9.02 | 8.98 | 8.97 | 9.21 | 9.08 | 9.13 | 9.04 | 8.71 | 9.35 | 8.84 | 8.56 | 8.89 | 9.11 | 8.84 | 8.97 | 9.21 | 8.85 | 8.33 | 8.66 | 8.23 | 8.59 | 8.13 | 7.79 | 9.11 | 7.91 |
| **MnO** | 0.11 | 0.13 | 0.11 | 0.11 | 0.12 | 0.12 | 0.13 | 0.13 | 0.12 | 0.12 | 0.12 | 0.12 | 0.11 | 0.12 | 0.11 | 0.11 | 0.11 | 0.12 | 0.11 | 0.12 | 0.08 | 0.10 | 0.11 | 0.11 | 0.09 | 0.08 | 0.11 | 0.10 | 0.09 | 0.11 |
| **MgO** | 41.89 | 40.91 | 41.09 | 40.81 | 41.26 | 40.95 | 41.22 | 40.72 | 41.18 | 41.45 | 43.51 | 44.76 | 45.18 | 46.16 | 45.88 | 47.25 | 46.92 | 45.24 | 44.96 | 46.04 | 49.51 | 49.68 | 50.11 | 48.91 | 49.54 | 49.87 | 48.99 | 49.27 | 49.12 | 49.49 |
| **CaO** | 2.16 | 2.31 | 2.22 | 2.08 | 2.34 | 2.55 | 2.13 | 2.36 | 2.35 | 2.12 | 1.38 | 0.77 | 0.55 | 0.28 | 0.35 | 0.59 | 0.96 | 0.61 | 0.57 | 0.74 | 0.09 | 0.18 | 0.14 | 0.25 | 0.21 | 0.12 | 0.24 | 0.22 | 0.25 | 0.24 |
| **$Na_2O$** | 0.04 | 0.06 | 0.02 | 0.04 | 0.01 | 0.03 | 0.04 | 0.07 | 0.03 | 0.05 | 0.02 | 0.01 | 0.01 | <0.01 | <0.01 | 0.01 | 0.01 | 0.01 | <0.01 | 0.02 | <0.01 | <0.01 | <0.01 | <0.01 | <0.01 | <0.01 | <0.01 | <0.01 | <0.01 | <0.01 |
| **$K_2O$** | 0.01 | 0.01 | 0.01 | <0.01 | 0.02 | <0.01 | <0.01 | <0.01 | 0.02 | <0.01 | <0.01 | <0.01 | <0.01 | <0.01 | <0.01 | <0.01 | <0.01 | <0.01 | <0.01 | <0.01 | <0.01 | <0.01 | <0.01 | <0.01 | <0.01 | <0.01 | <0.01 | <0.01 | <0.01 | <0.01 |
| **Total** | 100.6 | 98.69 | 100.1 | 98.31 | 99.82 | 98.73 | 98.49 | 99.19 | 99.44 | 99.40 | 99.59 | 98.74 | 99.69 | 99.96 | 99.15 | 100.1 | 101.6 | 99.14 | 98.83 | 100.1 | 98.92 | 99.52 | 98.87 | 98.05 | 98.47 | 99.57 | 98.07 | 98.18 | 98.15 | 98.20 |
| **LOI** | 5.74 | 3.26 | 1.57 | 6.31 | 8.43 | 7.16 | 4.21 | 2.09 | 7.98 | 8.44 | 10.25 | 9.76 | 10.22 | 12.45 | 6.49 | 4.12 | 11.33 | 12.22 | 8.91 | 8.69 | 8.99 | 9.19 | 9.44 | 13.03 | 5.17 | 6.61 | 10.81 | 13.66 | 5.22 | 11.06 |
| **Mg#** | 83.7 | 83.6 | 83.3 | 83.5 | 83.4 | 83.5 | 83.6 | 83.5 | 83.3 | 83.5 | 84.1 | 84.6 | 85.2 | 84.6 | 85.2 | 86.0 | 85.4 | 84.7 | 85.0 | 85.1 | 85.7 | 86.2 | 87.0 | 86.3 | 87.0 | 86.6 | 87.0 | 87.6 | 85.7 | 87.4 |
| **Trace Elements (ppm)** | | | | | | | | | | | | | | | | | | | | | | | | | | | | | | |
| **Sc** | 14.56 | 14.22 | 13.38 | 15.09 | 15.61 | 15.85 | 14.98 | 13.86 | 14.65 | 15.42 | 10.91 | 11.52 | 9.79 | 7.55 | 10.36 | 9.48 | 14.82 | 8.67 | 11.05 | 8.88 | 4.91 | 4.14 | 4.84 | 5.29 | 5.22 | 4.55 | 5.11 | 5.08 | 4.59 | 4.99 |
| **V** | 65.59 | 59.81 | 59.33 | 62.94 | 52.16 | 56.74 | 61.63 | 60.44 | 60.72 | 57.12 | 27.86 | 36.59 | 22.65 | 20.72 | 28.21 | 12.98 | 33.17 | 41.29 | 26.43 | 17.63 | 10.26 | 9.88 | 10.19 | 9.55 | 9.79 | 10.02 | 10.11 | 8.99 | 9.74 | 9.36 |
| **Cr** | 3349 | 3241 | 2916 | 2664 | 2819 | 2891 | 3187 | 2769 | 3271 | 3108 | 2538 | 2961 | 1189 | 1599 | 2675 | 2801 | 3445 | 3111 | 1851 | 3241 | 951 | 739 | 516 | 1004 | 863 | 913 | 1081 | 899 | 936 | 945 |
| **Co** | 98.53 | 102.3 | 99.11 | 97.55 | 104.8 | 98.22 | 102.4 | 96.25 | 99.91 | 101.1 | 98.66 | 116.7 | 114.1 | 97.24 | 108.7 | 102.9 | 105.7 | 113.2 | 104.4 | 110.3 | 94.54 | 97.81 | 89.82 | 110.6 | 96.29 | 113.8 | 106.2 | 99.18 | 111.2 | 98.12 |
| **Ni** | 2129 | 2554 | 2735 | 2172 | 2699 | 2049 | 2408 | 2635 | 2116 | 2630 | 2824 | 2756 | 3345 | 2519 | 2925 | 3239 | 3075 | 2209 | 2769 | 3117 | 3598 | 2876 | 3453 | 3708 | 2741 | 3159 | 2945 | 3725 | 3063 | 3423 |
| **Cu** | 29.28 | 31.69 | 27.59 | 24.72 | 19.14 | 22.94 | 25.66 | 21.77 | 25.16 | 20.58 | 7.49 | 9.59 | 14.22 | 8.58 | 21.28 | 5.18 | 2.19 | 18.02 | 1.95 | 13.44 | 8.54 | 1.99 | 5.18 | 1.71 | 4.16 | 3.22 | 3.56 | 4.68 | 6.88 | 2.39 |
| **Zn** | 46.71 | 44.72 | 45.99 | 44.12 | 41.45 | 44.39 | 42.64 | 39.15 | 42.88 | 45.08 | 38.77 | 46.16 | 37.45 | 40.83 | 32.61 | 31.64 | 39.98 | 41.16 | 35.51 | 35.84 | 25.77 | 24.16 | 32.18 | 27.69 | 29.42 | 31.21 | 34.33 | 29.37 | 31.62 | 28.92 |
| **Ga** | 1.984 | 2.031 | 1.574 | 1.843 | 1.478 | 1.835 | 2.061 | 1.642 | 1.742 | 1.658 | 0.246 | 0.687 | 0.311 | 0.278 | 0.710 | 0.545 | 0.455 | 0.454 | 0.682 | 0.491 | 0.218 | 0.171 | 0.111 | 0.206 | 0.168 | 0.197 | 0.151 | 0.191 | 0.125 | 0.148 |
| **Rb** | 0.086 | 0.728 | 0.541 | 0.067 | 0.226 | 1.119 | 0.662 | 1.098 | 0.822 | 0.491 | 0.125 | 0.087 | 0.025 | 0.047 | 0.038 | 0.128 | 0.071 | 0.201 | 0.185 | 0.094 | 0.045 | 0.053 | 0.026 | 0.041 | 0.038 | 0.013 | 0.039 | 0.023 | 0.019 | 0.033 |
| **Sr** | 0.991 | 4.636 | 0.122 | 0.851 | 0.085 | 0.759 | 1.399 | 0.612 | 2.787 | 1.902 | 0.247 | 1.416 | 0.174 | 0.997 | 0.049 | 0.121 | 0.035 | 0.876 | 1.208 | 0.084 | 0.096 | 0.108 | 0.041 | 0.074 | 0.066 | 0.035 | 0.311 | 0.053 | 0.222 | 0.179 |
| **Y** | 1.675 | 1.253 | 1.486 | 0.799 | 1.347 | 1.225 | 1.511 | 0.999 | 1.162 | 1.286 | 0.112 | 0.144 | 0.065 | 0.357 | 0.136 | 0.048 | 0.107 | 0.026 | 0.224 | 0.039 | 0.021 | 0.024 | 0.016 | 0.026 | 0.022 | 0.014 | 0.021 | 0.018 | 0.025 | 0.019 |
| **Zr** | 0.111 | 0.079 | 0.075 | 0.092 | 0.044 | 0.047 | 0.058 | 0.082 | 0.067 | 0.099 | 0.011 | 0.019 | 0.037 | 0.021 | 0.066 | 0.009 | 0.028 | 0.044 | 0.023 | 0.053 | 0.178 | 0.049 | 0.058 | 0.008 | 0.026 | 0.018 | 0.078 | 0.201 | 0.065 | 0.099 |
| **Nb** | 0.220 | 0.098 | 0.148 | 0.331 | 0.014 | 0.198 | 0.018 | 0.032 | 0.037 | 0.176 | 0.531 | 0.011 | 1.999 | 0.308 | 4.875 | 1.513 | 0.099 | 3.642 | 0.712 | 1.218 | 0.119 | 0.092 | 0.327 | 0.244 | 0.064 | 0.208 | 0.016 | 0.010 | 0.171 | 0.082 |
| **Cs** | 0.097 | 0.069 | 0.014 | 0.091 | 0.086 | 0.061 | 0.101 | 0.039 | 0.043 | 0.022 | 0.008 | 0.015 | 0.020 | 0.003 | 0.012 | 0.005 | 0.007 | 0.018 | 0.011 | 0.013 | 0.002 | 0.008 | 0.002 | 0.005 | 0.006 | 0.001 | 0.008 | 0.005 | 0.001 | 0.003 |
| **Ba** | 0.059 | 0.489 | 0.113 | 0.157 | 0.098 | 0.218 | 0.279 | 0.050 | 0.291 | 0.326 | 1.213 | 0.736 | 0.195 | 0.377 | 0.955 | 0.013 | 0.346 | 1.051 | 0.555 | 0.239 | 0.049 | 0.229 | 0.022 | 0.058 | 0.116 | 0.033 | 0.315 | 0.099 | 0.301 | 0.201 |
| **La** | 0.003 | 0.003 | 0.001 | 0.001 | 0.004 | 0.001 | 0.001 | 0.001 | 0.003 | 0.005 | 0.003 | 0.001 | 0.001 | 0.005 | 0.004 | 0.001 | 0.003 | 0.002 | 0.001 | 0.003 | 0.002 | 0.006 | 0.004 | 0.006 | 0.001 | 0.003 | 0.002 | 0.005 | 0.004 | 0.002 |
| **Ce** | 0.002 | 0.004 | 0.004 | 0.001 | 0.007 | 0.001 | 0.008 | 0.003 | 0.002 | 0.006 | 0.002 | 0.003 | 0.001 | 0.003 | 0.011 | 0.009 | 0.008 | 0.015 | 0.013 | 0.005 | 0.003 | 0.005 | 0.010 | 0.002 | 0.010 | 0.012 | 0.004 | 0.014 | 0.009 | 0.009 |
| **Pr** | 0.003 | 0.002 | 0.003 | 0.002 | 0.001 | 0.003 | 0.001 | 0.003 | 0.002 | 0.001 | 0.002 | 0.002 | 0.001 | 0.001 | 0.000 | 0.002 | 0.001 | 0.001 | 0.001 | 0.002 | 0.001 | 0.001 | 0.001 | 0.002 | 0.001 | 0.001 | 0.002 | 0.002 | 0.001 | 0.002 |
| **Nd** | 0.026 | 0.025 | 0.016 | 0.027 | 0.004 | 0.018 | 0.032 | 0.034 | 0.030 | 0.027 | 0.002 | 0.003 | 0.001 | 0.002 | 0.011 | 0.005 | 0.006 | 0.004 | 0.009 | 0.008 | 0.003 | 0.007 | 0.003 | 0.005 | 0.001 | 0.006 | 0.006 | 0.003 | 0.003 | 0.002 |
| **Sm** | 0.033 | 0.043 | 0.023 | 0.041 | 0.009 | 0.032 | 0.010 | 0.037 | 0.017 | 0.028 | 0.003 | 0.002 | 0.004 | 0.002 | 0.001 | 0.004 | 0.002 | 0.002 | 0.003 | 0.004 | 0.002 | 0.002 | 0.002 | 0.002 | 0.002 | 0.001 | 0.001 | 0.002 | 0.002 | 0.002 |
| **Eu** | 0.017 | 0.017 | 0.014 | 0.005 | 0.012 | 0.022 | 0.015 | 0.018 | 0.014 | 0.016 | 0.001 | 0.001 | 0.001 | 0.001 | 0.001 | 0.001 | 0.001 | 0.001 | 0.001 | 0.002 | 0.001 | 0.001 | 0.000 | 0.000 | 0.001 | 0.001 | 0.000 | 0.001 | 0.002 | 0.001 |
| **Gd** | 0.115 | 0.084 | 0.099 | 0.087 | 0.038 | 0.051 | 0.112 | 0.121 | 0.100 | 0.120 | 0.004 | 0.002 | 0.001 | 0.003 | 0.009 | 0.001 | 0.003 | 0.001 | 0.011 | 0.005 | 0.001 | 0.001 | 0.001 | 0.001 | 0.001 | 0.001 | 0.001 | 0.001 | 0.001 | 0.001 |
| **Tb** | 0.027 | 0.021 | 0.011 | 0.023 | 0.016 | 0.029 | 0.018 | 0.019 | 0.023 | 0.025 | 0.001 | 0.001 | 0.002 | 0.004 | 0.001 | 0.001 | 0.001 | 0.003 | 0.000 | 0.001 | 0.001 | 0.001 | 0.001 | 0.001 | 0.001 | 0.000 | 0.001 | 0.000 | 0.001 | 0.000 |
| **Dy** | 0.208 | 0.193 | 0.211 | 0.092 | 0.165 | 0.186 | 0.220 | 0.200 | 0.114 | 0.155 | 0.014 | 0.010 | 0.039 | 0.022 | 0.012 | 0.002 | 0.024 | 0.006 | 0.033 | 0.020 | 0.007 | 0.006 | 0.001 | 0.002 | 0.008 | 0.006 | 0.003 | 0.003 | 0.004 | 0.003 |
| **Ho** | 0.039 | 0.054 | 0.035 | 0.048 | 0.025 | 0.051 | 0.042 | 0.052 | 0.029 | 0.039 | 0.002 | 0.003 | 0.005 | 0.007 | 0.011 | 0.006 | 0.001 | 0.007 | 0.010 | 0.004 | 0.001 | 0.001 | 0.001 | 0.001 | 0.001 | 0.001 | 0.001 | 0.007 | 0.001 | 0.001 |
| **Er** | 0.121 | 0.153 | 0.158 | 0.086 | 0.125 | 0.099 | 0.148 | 0.166 | 0.135 | 0.120 | 0.008 | 0.018 | 0.017 | 0.043 | 0.013 | 0.001 | 0.032 | 0.003 | 0.019 | 0.021 | 0.003 | 0.003 | 0.003 | 0.002 | 0.003 | 0.002 | 0.003 | 0.002 | 0.003 | 0.002 |
| **Tm** | 0.026 | 0.029 | 0.018 | 0.024 | 0.016 | 0.025 | 0.027 | 0.20 | 0.029 | 0.028 | 0.004 | 0.003 | 0.004 | 0.004 | 0.002 | 0.001 | 0.003 | 0.003 | 0.001 | 0.002 | 0.001 | 0.001 | 0.001 | 0.001 | 0.001 | 0.001 | 0.000 | 0.001 | 0.001 | 0.001 |
| **Yb** | 0.189 | 0.154 | 0.176 | 0.115 | 0.169 | 0.192 | 0.194 | 0.133 | 0.151 | 0.161 | 0.013 | 0.064 | 0.031 | 0.010 | 0.023 | 0.006 | 0.022 | 0.055 | 0.034 | 0.016 | 0.007 | 0.007 | 0.006 | 0.008 | 0.007 | 0.006 | 0.006 | 0.007 | 0.008 | 0.007 |
| **Lu** | 0.024 | 0.035 | 0.034 | 0.029 | 0.022 | 0.031 | 0.026 | 0.029 | 0.034 | 0.30 | 0.013 | 0.005 | 0.007 | 0.005 | 0.002 | 0.012 | 0.004 | 0.013 | 0.010 | 0.008 | 0.002 | 0.002 | 0.002 | 0.002 | 0.002 | 0.002 | 0.002 | 0.002 | 0.002 | 0.002 |
| **Hf** | 0.009 | 0.019 | 0.013 | 0.007 | 0.017 | 0.013 | 0.012 | 0.018 | 0.017 | 0.005 | 0.003 | 0.002 | 0.002 | 0.001 | 0.001 | 0.002 | 0.002 | 0.001 | 0.003 | 0.003 | 0.003 | 0.007 | 0.005 | 0.004 | 0.005 | 0.001 | 0.003 | 0.001 | 0.002 | 0.006 |
| **Ta** | 0.002 | 0.001 | 0.002 | 0.003 | 0.003 | 0.002 | 0.003 | 0.002 | 0.002 | 0.002 | 0.003 | 0.002 | 0.002 | 0.008 | 0.008 | 0.001 | 0.006 | 0.004 | 0.005 | 0.005 | 0.003 | 0.002 | 0.005 | 0.002 | 0.004 | 0.001 | 0.005 | 0.002 | 0.004 | 0.005 |
| **Pb** | 0.035 | 0.164 | 0.072 | 0.144 | 0.100 | 0.006 | 0.114 | 0.052 | 0.022 | 0.101 | 0.100 | 0.219 | 0.003 | 0.032 | 0.018 | 0.643 | 0.023 | 0.010 | 0.120 | 0.091 | 0.093 | 0.008 | 0.056 | 0.774 | 0.065 | 1.792 | 0.199 | 0.018 | 0.026 | 0.018 |
| **Th** | 0.001 | 0.001 | 0.001 | 0.001 | 0.001 | 0.001 | 0.001 | 0.001 | 0.001 | 0.000 | 0.001 | 0.009 | 0.001 | 0.002 | 0.001 | 0.001 | 0.001 | 0.001 | 0.001 | 0.001 | 0.007 | 0.002 | 0.001 | 0.001 | 0.001 | 0.001 | 0.010 | 0.001 | 0.004 | 0.002 |
| **U** | 0.001 | 0.001 | 0.001 | 0.001 | 0.001 | 0.001 | 0.001 | 0.001 | 0.001 | 0.001 | 0.002 | 0.001 | 0.001 | 0.001 | 0.001 | 0.001 | 0.001 | 0.002 | 0.002 | 0.001 | 0.001 | 0.001 | 0.001 | 0.002 | 0.000 | 0.001 | 0.001 | 0.001 | 0.001 | 0.001 |
| **K** | 22.16 | 16.13 | 19.84 | 19.56 | 16.69 | 17.33 | 22.08 | 21.91 | 20.36 | 21.44 | 11.42 | 15.11 | 12.56 | 13.18 | 10.92 | 15.23 | 12.83 | 13.16 | 10.44 | 14.09 | 4.49 | 7.36 | 2.95 | 3.98 | 5.33 | 4.12 | 2.73 | 6.78 | 3.56 | 5.23 |
| **Ti** | 81.53 | 77.56 | 75.18 | 71.36 | 94.42 | 84.47 | 87.13 | 101.0 | 72.38 | 98.27 | 42.54 | 39.67 | 33.94 | 22.78 | 65.16 | 16.53 | 16.97 | 12.19 | 43.08 | 27.08 | 14.13 | 17.55 | 44.26 | 14.23 | 10.11 | 11.96 | 12.37 | 23.16 | 15.72 | 35.46 |

*Note*: LOI-loss on ignition.

Os (Li et al., 2014, Li et al., 2015). The total operational blanks were about 3 pg for Re and 0.5 pg for Os based on blank runs tested alongside the samples.

## 5. Mineral compositions

### 5.1. Olivine

Olivine compositions in Dargai peridotites largely reflect the whole-rock lithologies (Table 1). In the Cpx-harzburgites the forsterite values range from 89.8 to 90.4, which are lower than those in the depleted harzburgites and dunites (91.0 to 91.6 and 92.2 to 92.8, respectively). The NiO contents vary positively with the Fo values, from 0.38 to 0.42 wt% in the Cpx-harzburgites to 0.35–0.45 wt% in the depleted harzburgites and (0.41–0.44 wt%) in the dunites (Fig. 4a).

### 5.2. Orthopyroxene

Orthopyroxene grains in the depleted harzburgite samples are mostly fresh, but some are partially altered or replaced by bastite in a few highly altered samples. Most grains are subhedral porphyroblasts ~5 mm long, although minute, anhedral grains are commonly present in the matrix. Exsolution lamellae of clinopyroxene are observed in some of the large porphyroblasts (Fig. 3a–c). Sparse grains of orthopyroxene in the Cpx-harzburgites have enstatite (En) values of 86.7 to 89.1, whereas in the depleted harzburgites and dunites the En values are 89.5 to 90.4 and 89.3 to 91.3 (Table 2), respectively. Hence, the En values of the orthopyroxene correlate positively with increasing depletion of the peridotites. Their Mg# [100 * Mg /(Mg + Fe)] values range from 89.7 to 90.6 in the Cpx-harzburgites, from 91.2 to 91.8 in the depleted harzburgites and from 91.8 to 92.5 in the dunites. The $Al_2O_3$ contents of the orthopyroxene are also variable, being in the range of 3.91 to 5.12 wt% in the Cpx-harzburgites, 1.11 to 2.16 wt% in the depleted harzburgites and 0.51 to 0.98 wt% in the dunites. Thus, the $Al_2O_3$ values correlate negatively with the En contents (Fig. 4b).

### 5.3. Clinopyroxene

Typically, clinopyroxene grains in the Cpx-harzburgites, depleted harzburgites, and dunites, are diopsidic in composition but have slightly different Mg# values (Table 3). Clinopyroxene in the Cpx-harzburgites has the lowest Mg# values (92.4–92.9) compared to those in the harzburgites (94.0 to 95.2) and dunites (94.8 to 96.1), all of which show a positive correlation with increasing degrees of depletion. The $Al_2O_3$ contents of the clinopyroxene is highest in the Cpx-harzburgite, ranging from 3.65 to 5.19 wt%; in the depleted harzburgites and dunites the contents are 1.08 to 3.29 wt% and 0.77 to 1.39 wt%, respectively (Fig. 4c). The $TiO_2$ contents in the clinopyroxene correlate negatively with the Mg# values, reaching a maximum value of 0.24 wt% in the Cpx-harzburgites and decreasing regularly to a minimum of 0.01 in the dunites.

Selected rare earth elements (REE) and other trace element compositions of the clinopyroxene in the Cpx-harzburgites and depleted harzburgites are presented in Table 5. The clinopyroxene in the Cpx-harzburgite samples have concave or spoon-like patterns with a notable enrichment in HEE and high field strength elements (HFSE) (Fig. 5a), and are similar to those of abyssal peridotites (Lian et al., 2018; Ullah et al., 2020a; Wu et al., 2018). In contrast, clinopyroxenes in the depleted harzburgites show a prominent depletion in HREE and HFSE (Fig. 5b), which again resembles those of abyssal peridotites. Clinopyroxene grains in both the Cpx-harzburgites and depleted harzburgites show significant enrichment in large ion lithophile elements (LILE) and display positive Pb and negative Zr and Sr anomalies on the spider diagram (Fig. 5a and b).

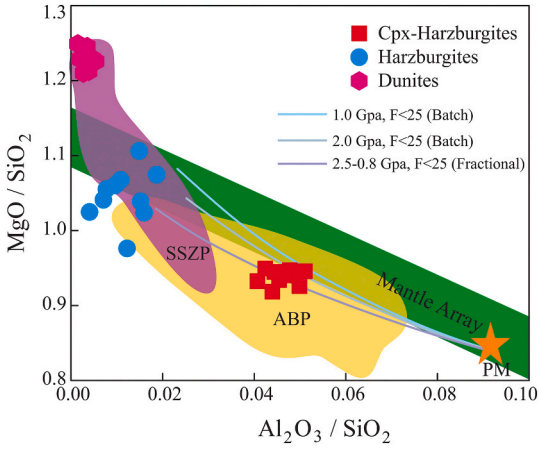


**Fig. 6.** Whole-rock $Al_2O_3$ and MgO concentrations of the Dargai peridotites normalized to $SiO_2$. The mantle array is taken from Wu et al. (2018). The data for Abyssal Peridotites (ABP) and isobaric batch and near fractional melting of a fertile mantle source (orange-star) are from Niu et al. (1997), and for Supra-Subduction Zone peridotites (SSZP) from Parkinson and Pearce (1998) and Ullah et al. (2020a). All the analyzed harzburgite and dunite samples plot within the SSZP field and Cpx-harzburgite within the ABP field.

### 5.4. Cr-Spinel

Residual grains of Cr-spinel are present in all of the Dargai peridotites. In serpentinized peridotites, most grains are altered to ferritchromite along rims and cracks but retain their original compositions in their cores. Thus, we focused on the fresh cores to obtain primary compositions Table 4. Both high-alumina and high-chrome varieties are present. The Cpx-peridotites contain the most aluminous varieties, which have $Al_2O_3$ concentrations of 48.1 to 53.9 wt%, Cr# [100*Cr/(Cr + Al)] values of 15.2–20.7, and Mg# values of 69.4–73.8. In the depleted harzburgites the Cr-spinels have intermediate alumina contents (11.9–36.8 wt%) and yield Cr# values of 38.4–74.8 and Mg# values of 45.6–63.4. In contrast, grains in the dunites have very low alumina (8.22 to 12.1 wt%) and high Cr# values of 75.0–81.9 with Mg# values of 37.4 to 43.9. The $TiO_2$ concentrations of the Cr-spinel range from a low of 0.04 wt% in the Cpx-harzburgites to a high of 0.11 wt% in the dunites, whereas NiO contents range from a low of 0.05 wt% in the depleted harzburgites and dunites to a high of 0.31 wt% in the Cpx-harzburgites. Clearly, both the Cr# and Mg# values correlate linearly with the degrees of depletion in the host lithologies and plot in the compositional fields for abyssal peridotites (ABP) and suprasubduction zone peridotites (SSZP) (Fig. 4d).

## 6. Whole-rock geochemistry

### 6.1. Major and trace elements

The loss-on ignition (LOI values for the whole-rock samples (1.57–13.7 wt%; Table 6) show that all of the examined peridotites and dunites are at least partially altered. However, most samples retain clear remnants of their primary textural and mineralogical features. In general, the dunites are less altered than the depleted harzburgites and Cpx-harzburgites, and mostly appear to have had varying degrees of late-stage refertilization. The dunite samples are Mg-rich (MgO: 40.7–50.1 wt%), Al-poor ($Al_2O_3$: 0.06–2.24 wt%), and extremely alkali-poor ($Na_2O$: <0.01–0.07 wt%). The low CaO contents (0.06–0.67 wt%) are conformable with the paucity of clinopyroxene in these rocks.

In the $MgO/SiO_2$ vs $Al_2O_3/SiO_2$ diagram (Fig. 6) the bulk compositions of the peridotites show a depletion pattern slightly below, but parallel to, the terrestrial mantle array (Lian et al., 2018; Ullah et al., 2020a; Wu et al., 2018). A noticeable depletion in the serpentinized

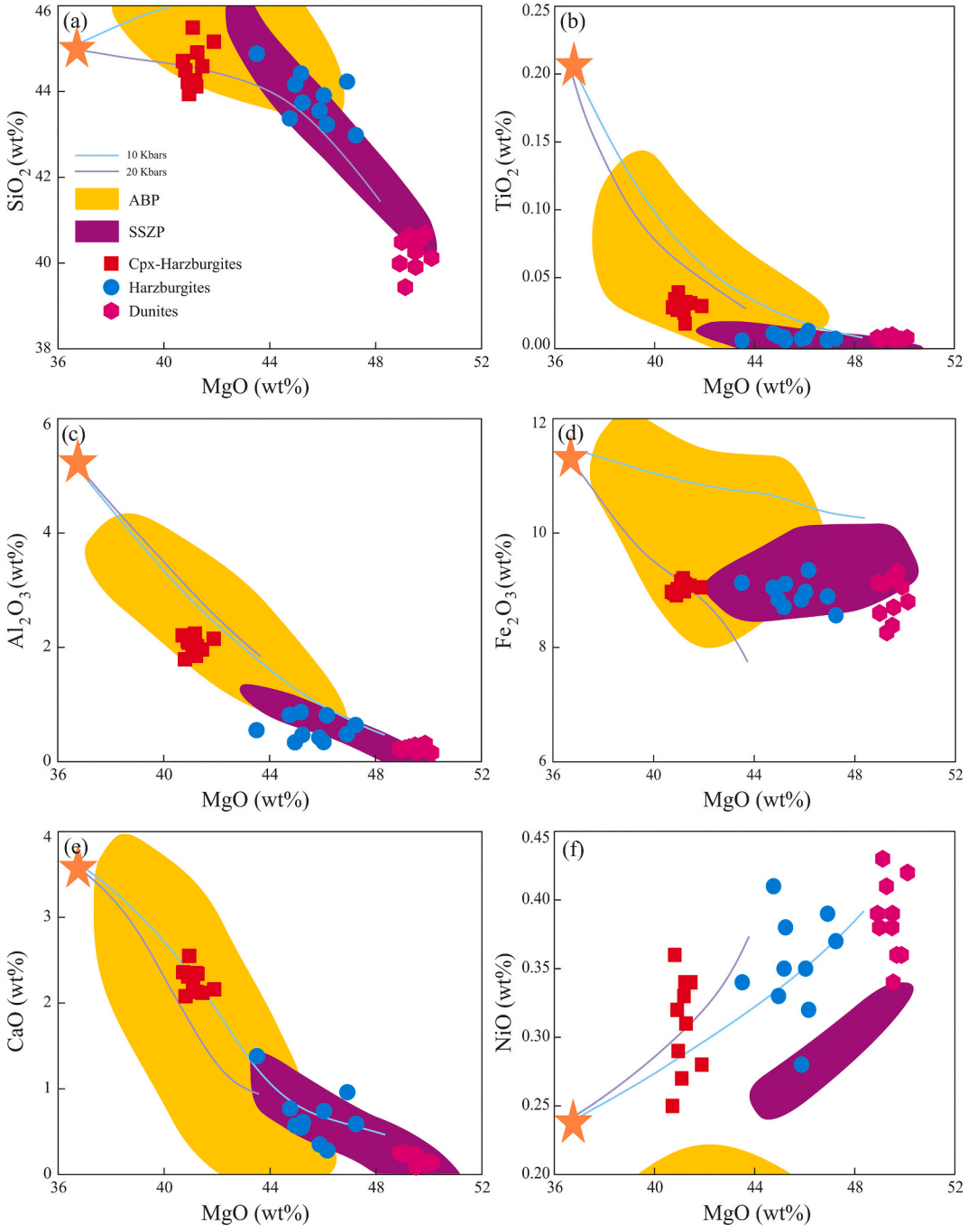


**Fig. 7.** Variation diagrams showing whole-rock compositional ranges of major oxides in peridotite samples from the Dargai peridotites. Compositions are calculated on a volatile-free basis. Abyssal and SSZ peridotite fields are from Niu et al. (1997) and Parkinson and Pearce (1998). The primitive mantle fields (orange stars) are taken from Palme and O'Neill (2013). Melting trends (blue and grey lines) at 10 and 20 kbar of primitive mantle are taken from Niu et al. (1997). (For interpretation of the references to colour in this figure legend, the reader is referred to the web version of this article.)

peridotites may reflect loss of magnesium or addition of $SiO_2$. During partial melting, the $Al_2O_3/SiO_2$ ratios in the clinopyroxene and orthopyroxene significantly decreased, whereas the $MgO/SiO_2$ ratios increased slightly. As melting progressed, pyroxene, particularly clinopyroxene was consumed, by a late-stage olivine-rich melt that change the Cpx-harzburgite to depleted harzburgite and dunite, causing increases in the bulk $MgO/SiO_2$ ratios. However, the relatively low $MgO/SiO_2$ ratios of the Cpx-harzburgite samples may reflect some loss of MgO (Fig. 6) by alteration (Lian et al., 2018; Niu, 2004; Snow and Dick, 1995; Wu et al., 2018). Likewise, the generally lower than expected abundances of major and trace elements for a given degree of melting might also have been due to alteration. Nonetheless, the MgO concentrations and the Mg# values of the depleted harzburgites and dunites remained relatively high. All the analyzed Cpx-harzburgites, which plot in the abyssal peridotite field, are characterized by low $MgO/SiO_2$ values, whereas the depleted harzburgites and dunites with high $MgO/SiO_2$ values all plot in the SSZ peridotite field, suggesting high-MgO parental magmas and/or late-stage melt-rock interaction (Fig. 6).

The contents of $TiO_2$, $Al_2O_3$, $Fe_2O_3$, $SiO_2$, and CaO of the Cpx-harzburgite samples are higher than those in the depleted harzburgites and dunites, whereas the NiO contents are lower (Table 6; Fig. 7). Mg# values of the Cpx-harzburgite samples, which are essentially constant

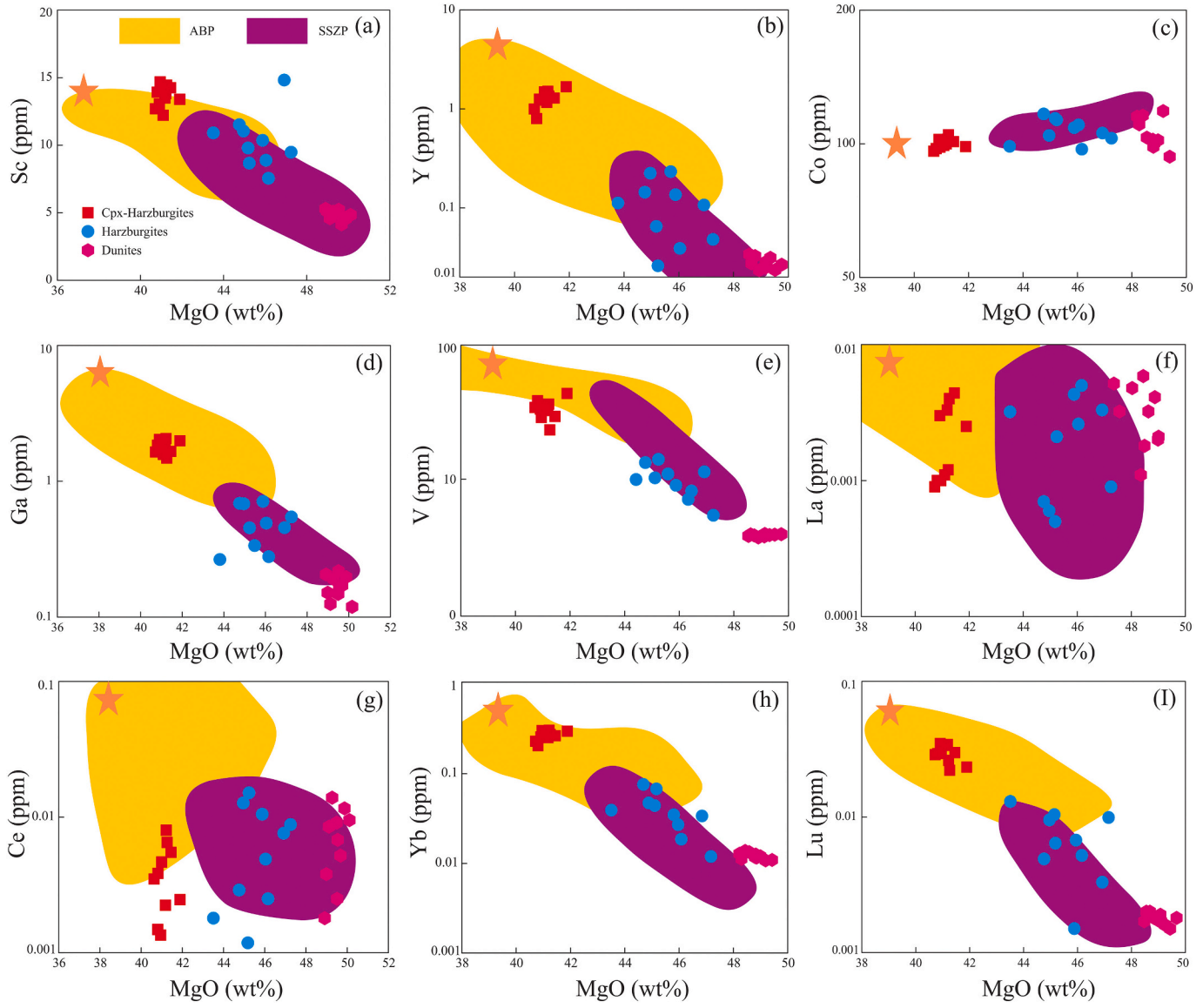


**Fig. 8.** Variation diagrams of MgO versus selected trace and rare earth elements in bulk-rock peridotite samples of the Dargai ophilite. Abyssal and SSZ peridotite fields are from Niu et al. (1997) and Parkinson and Pearce (1998). Primitive mantle fields (orange stars) are from Palme and O'Neill (2013), respectively.

(83.3 to 83.7), are slightly lower than the those of the depleted harzburgites (84.1–86.0) and dunites (85.7–87.6) (Table 6). The MgO contents correlate well with all the other elements except for Ce, La, Nb, and Ta (Niu et al., 1997; Parkinson and Pearce, 1998). Cobalt is compatible during partial melting, whereas the other elements are incompatible with olivine thus, Co correlates positively with MgO (Fig. 8). All of the REE (except for Ce and La) correlate negatively with MgO (Fig. 8). The chalcophile elements Cu and S behave identically to Al and Ca during partial melting (Luguet et al., 2003; Wu et al., 2018) thus, Cu decreases with increasing degrees of depletion (Table 6).

Comparison of the Dargai peridotites those of known tectonic environments shows that both the major and trace element abundances of the Cpx-harzburgites are comparable to MOR-types whereas the depleted harzburgites and dunites are closely akin to SSZ or forearc varieties. All the peridotites are characterized by variously depleted REE patterns (Fig. 5c and d). The REE concentrations of Lu to Ce are continuously depleted in the Cpx-harzburgite samples followed by a slight La enrichment (Fig. 5c). The depleted harzburgites and dunites are characterized by (1) lower HREE abundances, and (2) a sharper decline from HREE to MREE compared to the Cpx-harzburgite samples (Fig. 5d). The depleted harzburgite and dunite samples have similar light rare earth elements (LREE) concentrations, whereas the medium rare earth elements (MREE) and HREE abundances of the dunite samples are lower than those of the depleted harzburgite samples. The depleted harzburgites and dunites compare closely with SSZ peridotites with low REE concentrations, but have higher abundances of HREE (Fig. 5c and d).

The Cpx-harzburgites samples are characterized by a pronounced negative Ti anomaly, whereas the depleted harzburgite and dunite samples display slightly positive Ti anomalies. In addition, the Cpx-harzburgite samples are distinguished by a noticeable depletion in Zr, which is absent in the depleted harzburgite and dunite (Fig. 5d). The absence of a consistent relationship between LOI, Nb, and Sr implies that the Pb and Sr anomalies were not produced by serpentinization.

### 6.2. *Platinum group elements*

The total PGE concentrations in the Dargai peridotites are between 25.3 and 55.5 ppb, with an average of 34 ppb (Table 7). The Cpx-harzburgite samples display Pt anomalies (Pt/Pt* values of 2.25 to 0.96; this variation is likely reflects the heterogeneous distribution of

**Table 7**
PGE, Re concentrations (ppb) and *Re*-Os Isotopic data of the Dargai Complex peridotites.

| S. No | Cr# | Os | Ir | Ru | Rh | Pt | Pd | ΣPGE | Pd/Ir | Pt/Pt* | Re | Re* | Re/Os | $^{187}Os/^{188}Os$ | $^{187}Re/^{188}Os$ | $^{187}Os/^{188}Os$ at 250 Ma | γOs | $T_{RD}$/Ma | $T_{MA}$/Ma |
|---|---|---|---|---|---|---|---|---|---|---|---|---|---|---|---|---|---|---|---|
| **Cpx-H-1** | 18.8 | 4.98 | 3.04 | 7.98 | 1.91 | 8.99 | 9.94 | 36.84 | 3.27 | 1.78 | | | | | | | | | |
| **Cpx-H-2** | 16.1 | 4.45 | 4.11 | 5.92 | 1.24 | 8.44 | 7.33 | 31.49 | 1.78 | 1.16 | | | | | | | | | |
| **Cpx-H-3** | 15.2 | 2.01 | 4.16 | 8.11 | 1.96 | 7.29 | 11.9 | 35.51 | 2.88 | 1.61 | 0.38 | 0.2 | 0.189 | 0.12928 | 0.851 | 0.12827 | 1.76 | *f* | *f* |
| **Cpx-H-4** | 17.1 | 3.97 | 3.26 | 11.9 | 1.45 | 6.13 | 8.16 | 34.93 | 2.50 | 0.96 | | | | | | | | | |
| **Cpx-H-5** | 20.5 | 2.03 | 4.28 | 8.02 | 1.37 | 9.04 | 6.24 | 30.98 | 1.46 | 1.20 | 0.57 | 0.18 | 0.281 | 0.13098 | 1.391 | 0.12997 | 2.38 | *f* | *f* |
| **Cpx-H-6** | 16.6 | 4.19 | 3.12 | 7.74 | 2.01 | 13.45 | 6.76 | 37.27 | 2.17 | 2.25 | 0.42 | 0.2 | 0.100 | 0.12571 | 0.827 | 0.12495 | −0.76 | 271 | 373 |
| **Cpx-H-7** | 16.8 | 4.37 | 3.44 | 9.03 | 1.77 | 7.71 | 10.0 | 36.33 | 2.91 | 1.47 | | | | | | | | | |
| **Hrz-1** | 62.7 | 4.05 | 4.18 | 11.0 | 1.04 | 5.74 | 6.39 | 32.41 | 1.53 | 0.67 | 0.08 | 0 | 0.020 | 0.12624 | 0.104 | 0.12597 | −0.97 | 492 | 495 |
| **Hrz-2** | 75.2 | 4.92 | 4.99 | 4.14 | 1.59 | 7.92 | 31.9 | 55.52 | 6.40 | 2.56 | | | | | | | | | |
| **Hrz-3** | 38.4 | 6.14 | 3.62 | 9.42 | 3.03 | 6.66 | 11.9 | 40.85 | 3.31 | 1.82 | 1.92 | 0 | 0.313 | 0.11699 | 1.225 | 0.11699 | −5.31 | 1318 | 1318 |
| **Hrz-4** | 52.6 | 2.37 | 5.95 | 19.9 | 1.48 | 4.52 | 5.19 | 39.47 | 0.87 | 0.57 | 0.14 | 0.01 | 0.059 | 0.12173 | 0.281 | 0.12155 | −3.55 | 154 | 175 |
| **Hrz-5** | 74.8 | 8.95 | 2.61 | 8.33 | 3.14 | 13.05 | 1.03 | 37.11 | 0.39 | 1.07 | | | | | | | | | |
| **Hrz-6** | 49.1 | 3.63 | 4.14 | 10.9 | 2.16 | 8.59 | 8.22 | 37.72 | 1.99 | 1.64 | | | | | | | | | |
| **Hrz-7** | 53.2 | 5.56 | 3.97 | 7.71 | 1.43 | 9.01 | 10.2 | 37.83 | 2.56 | 1.56 | 0.17 | 0 | 0.031 | 0.12641 | 0.145 | 0.12612 | −0.96 | 258 | 258 |
| **Dn-1** | 78.6 | 3.91 | 4.18 | 7.21 | 1.58 | 5.27 | 4.03 | 26.18 | 0.96 | 0.60 | | | | | | | | | |
| **Dn-2** | 75.0 | 4.32 | 3.79 | 6.03 | 2.01 | 6.19 | 3.22 | 25.56 | 0.85 | 0.72 | | | | | | | | | |
| **Dn-3** | 81.9 | 3.69 | 4.95 | 6.18 | 1.84 | 5.48 | 4.15 | 26.29 | 0.84 | 0.69 | | | | | | | | | |
| **Dn-4** | 81.2 | 3.29 | 3.51 | 8.22 | 1.55 | 5.09 | 3.59 | 25.25 | 1.02 | 0.55 | | | | | | | | | |
| **Dn-5** | 76.8 | 4.16 | 3.44 | 7.55 | 1.61 | 5.57 | 3.08 | 25.41 | 0.90 | 0.56 | | | | | | | | | |
| **Dn-6** | 79.2 | 4.09 | 4.26 | 6.39 | 1.67 | 6.11 | 3.37 | 25.89 | 0.79 | 0.66 | | | | | | | | | |
| **Dn-7** | 78.9 | 3.96 | 4.31 | 6.88 | 1.79 | 5.81 | 3.49 | 26.24 | 0.81 | 0.66 | | | | | | | | | |

*Note*: γOs is calculated by using the values from Shirey and Walker (1998) and λ for $^{187}Re = 1.666 \times 10^{-11}$ $a^{-1}$ (Smoliar et al., 1996). *f*: future age.
$Pt/Pt^* = (Pt/8.3)/[(Rh/1.6) \times (Pd/4.4)]^{1/2}$.

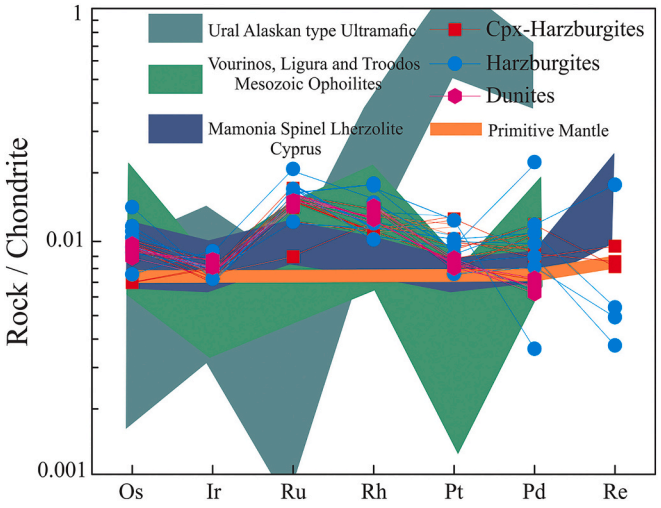


**Fig. 9.** Platinum group element (PGE) chondrite-normalized abundances of representative Cpx-harzburgites, harzburgites and dunites from the Dargai ophiolite. Primitive mantle values are from McDonough and Sun (1995). The comparison field of Mamonia spinel lherzolite is from Batanova et al. (2008). Data for Ural-Alaskan type ultra-mafic rocks and Vourinos, Ligura and Troodos ophiolite fields are from Garuti et al. (1997).

base metal minerals (BMM), in the system (González-Jiménez et al., 2011; Lorand et al., 2010; Prichard et al., 2008). Five of the 7 analyzed depleted harzburgites have slightly positive Pt anomalies (Pt/Pt*: 1.07–2.56), whereas the other 2 depleted harzburgites and all the dunites display negative Pt anomalies (Pt/Pt*: 0.55–0.72). In the Cpx-harzburgite samples Pd/Ir ratios range from 1.46 to 3.27 (Table 7). These data yield a slightly positive pattern from Os to Pd in the mantle-normalized PGE diagram (Fig. 9). The harzburgite and dunite samples have Pd/Ir values 0.39–6.40, revealing a wider range of values than the Cpx-harzburgite samples. Therefore, in chondrite normalized PGE plots, the depleted harzburgite and dunite samples show positive pattern from Os to Rh and a negative pattern from Rh to Pt, although some samples are also characterized by positive to negative anomalies from Pt to Pd.

Almost all the analyzed samples have patterns similar to those Greek ophiolites (e.g. Troodos and Vourinos) (Fig. 9), but different from the Mirdita ophiolite in Albania and the Aladag ophiolite in Turkey (Lian et al., 2018; Wu et al., 2018). One of our harzburgite samples shows a positive pattern with a Pd/Ir value of 6.4, and is slightly enriched in Cu (21 ppm), which may indicate the presence of some Cu-rich sulfides (Bockrath et al., 2004; Lorand et al., 2010; Marchesi et al., 2013; Wu et al., 2018). When the PGE concentrations of the Dargai samples are modelled against their $Al_2O_3$ values during partial melting of primitive upper mantle using concentrations of McDonough and Sun (1995) (Fig. 10) the two show a negative correlation.

### 6.3. *Re-Os isotopic composition*

Analyzed samples of the Dargai Cpx-harzburgites and depleted harzburgites have concentrations of Os and Re ranging from 2.01 to 6.16 ppb and 0.05 to 1.92 ppb, respectively (Table 7). All the depleted harzburgites and one Cpx-harzburgite have $^{187}Os/^{188}Os$ ratios ranging from 0.11699 to 0.12699, values that are lower than those of the present-day primitive mantle (0.1296; Meisel et al., 2001) and of chondrites (0.1275; Walker et al., 1989). Two of the Cpx-harzburgite samples have $^{187}Os/^{188}Os$ ratios (0.12928 and 0.13098) that are very close to the present-day primitive mantle value and greater than the chondritic value. The $^{187}Os/^{188}Os_{(i)}$ compositions of the Cpx-harzburgite samples are 0.12495 to 0.12997 (γOs = − 0.76 to +1.76) and the derived age of 250 Ma, corresponds generally to the opening of Neo-Tethys in the eastern Mediterranean region (Lapierre et al., 2004).

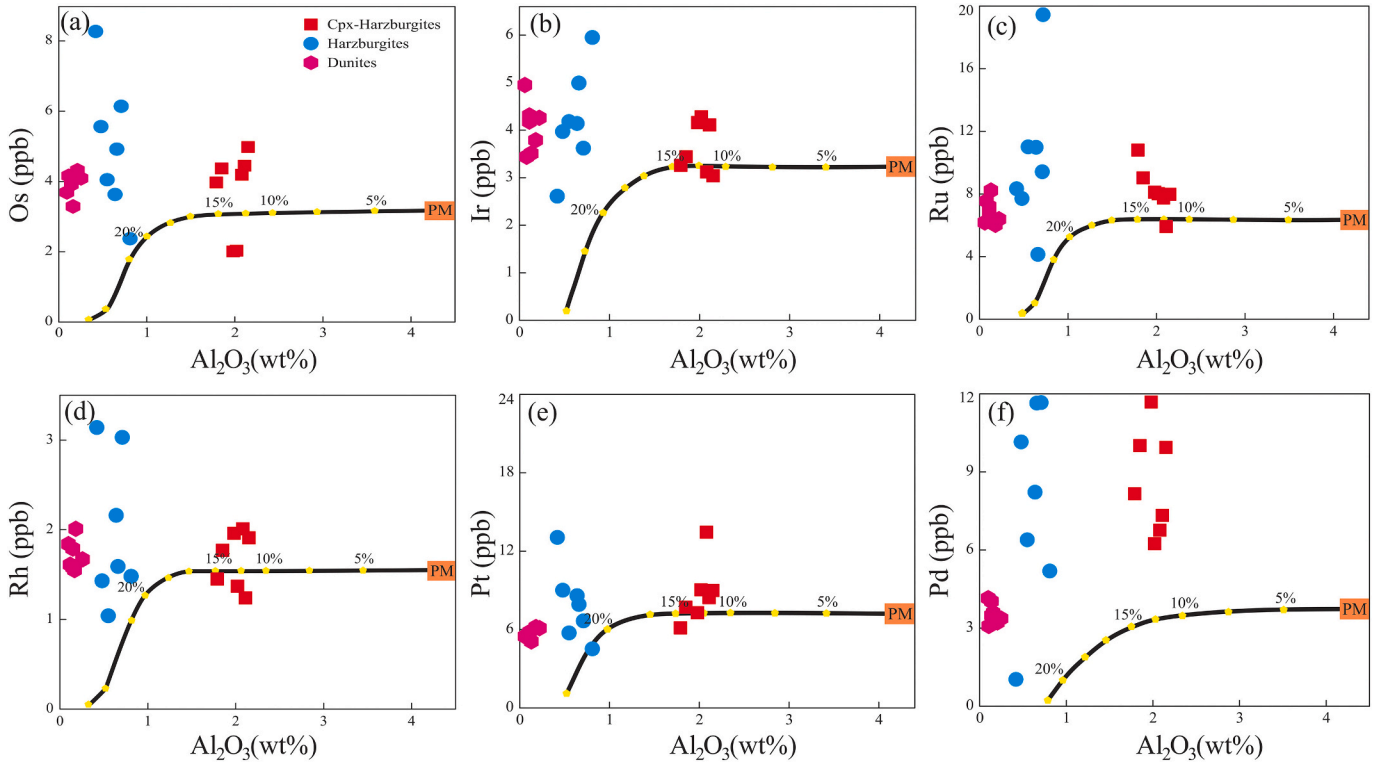


**Fig. 10.** Plot of Os, Ir, Ru, Rh, and Pt versus $Al_2O_3$ (wt%) of the Dargai Complex peridotites. Primitive mantle values (PM) and melting curves are from Marchesi et al. (2013) and McDonough and Sun (1995). Dots on melt extraction curves shows melting addition in percent. See text for discussion.

However, the $^{187}Os/^{188}Os_{(i)}$ ratios of the depleted harzburgites are slightly lower, ranging from 0.11699 to 0.12612 ($\gamma Os = -5.31$ to $-0.96$). The samples have Cpx-harzburgite slightly higher values of $^{187}Os/^{188}Os_{(i)}$ (for 250 Ma) than the depleted harzburgites, revealing a negative correlation between $^{187}Os/^{188}Os_{(i)}$ and Cr# values of the Cr-spinels (Fig. 11b).

Rhenium concentrations in the Dargai ophiolite plot above the depletion line revealing a negative correlation between Re and $Al_2O_3$ contents (Fig. 11a), that suggests later modification, which precludes Os isotope dating of the analyzed peridotites (Fig. 11c). The Cpx-harzburgite samples have $^{187}Re/^{188}Os$ values (0.827–1.391) that are higher than those of the depleted harzburgite samples (0.104–1.225) and primitive mantle (~ 0.40; Meisel et al., 2001).

## 7. Discussion

### 7.1. Degrees of partial melting and their implications

The Cpx contents of ophiolitic peridotites reflect only the degree of depletion (Uysal et al., 2012). Because the equilibrium between olivine and melt remains unchanged by input of $H_2O$ (Gaetani and Grove, 1998), Fo values the olivine can be used as an approximation of the total partial melting temperature (Ballhaus et al., 1991; Lian et al., 2018; Wu et al., 2018). Using our olivine compositional data, we infer that the Dargai ophiolite, which contains variable amounts of clinopyroxene (up to 5 vol%) and olivine with high forsteritic contents (89.8–92.8), underwent varying degrees of partial melting (Lian et al., 2018; Ullah et al., 2020a, 2020b; Wu et al., 2018). The Al concentrations of spinel and pyroxene are sensitive to the degrees of partial melting in mantle rocks and both decrease as the peridotites become more depleted (Dick and Natland, 1996; Uysal et al., 2015; Zhou et al., 2005). The $Al_2O_3$ values of clinopyroxene in the Dargai peridotites correlate negatively with the Cr# values of spinel with which they were equilibrated. Thus, the high $Al_2O_3$ contents of the clinopyroxene in the Cpx-harzburgites are associated with low-Cr spinels (Fig. 12a). Variations in $Al_2O_3$ versus $TiO_2$ values in clinopyroxene in the Cpx-harzburgites, depleted harzburgites, and dunites are consistent with an increasing degrees of partial melting (Fig. 12b). In addition, the Cr# and Mg# values of the Cr-spinels in these peridotites correlate negatively, suggesting that they contain both $Fe^{2+}$ and $Fe^{3+}$, which provides some evidence of the redox state of rocks and magmas (Ballhaus et al., 1991). A good correlation between spinel Cr# and olivine Mg# values in the peridotites indicates that the studied samples plot within the olivine-spinel mantle array (Arai, 1992). These data suggest that the peridotites underwent two stages of melt extraction, the first producing the Cpx-harzburgites and the second (the depleted harzburgites and dunites: (Fig. 12c). Therefore, we suggest that the Cpx-harzburgites of the Dargai Complex are the residues after low degrees of partial melting in a MOR setting, whereas the depleted harzburgites and dunites were derived from re-melting of the Cpx-harzburgites in a SSZ setting (Fig. 12c).

### 7.2. Oxygen fugacity ($fO_2$) of the peridotites

The $fO_2$ of peridotites during partial melting can be easily quantified by applying the thermometers of coexisting chromian spinel (Mg-Fe exchange), olivine, and orthopyroxene (Ballhaus et al., 1991; Lian et al., 2018; Wu et al., 2018). In order to determine the values of $fO_2$ on the basis of microprobe analyses of the minerals, we used the formula of Ballhaus et al. (1991), which is based on the following reaction;

$$6\ Fe_2SiO_4\ (olivine) + O_2\ (fluid) = 3\ Fe_2Si_2O_6\ (Opx) + 2\ Fe_3O_4\ (spinel)$$

Oxygen fugacity values have been calculated based on average mineral compositions which are given in Table 8, as deviations ($\Delta \log fO_2^{FMQ}$) from the FMQ (fayalite-magnetite-quartz) buffer (Fig. 13a). Mantle wedge peridotites above subduction zones are more oxidized compared to upper mantle peridotites in other tectonic environments (Parkinson and Arculus, 1999) due to the important role played by water in these enviroments (Arculus, 1994). The measured $fO_2$ for the depleted

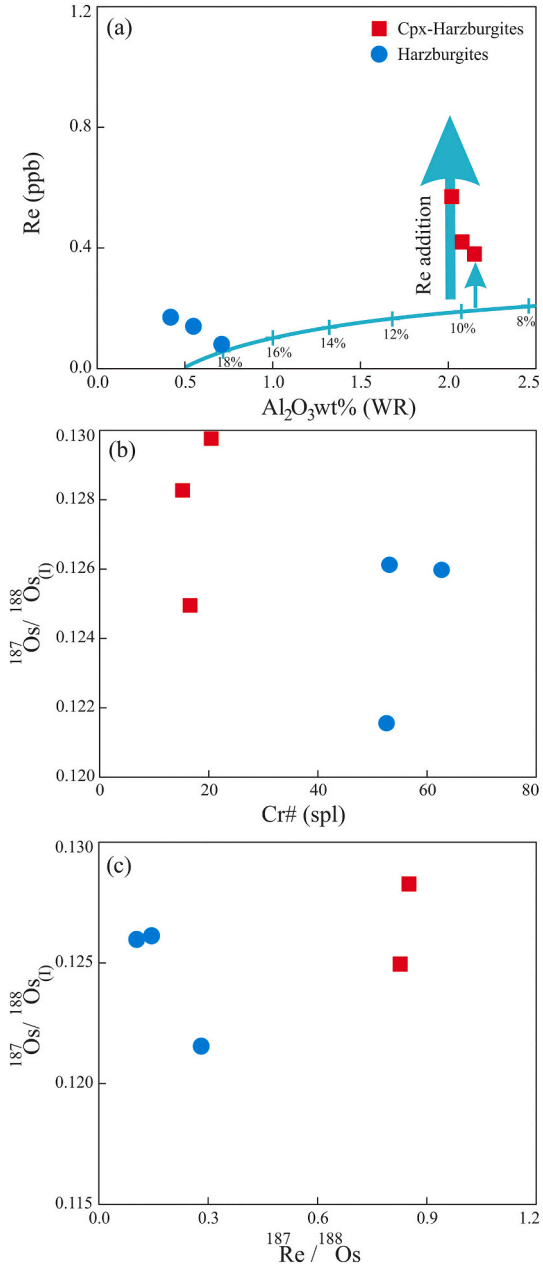


**Fig. 11.** (a) Whole-rock $Al_2O_3$ versus Re (ppb) of selected peridotite samples; (b) Cr# of chromite versus whole-rock $^{187}Os/^{188}Os_{(I)}$; and (c) $^{187}Re/^{188}Os_{(I)}$ versus $^{187}Re/^{188}Os$ of selected peridotite samples. The depletion trend in "a" shows the result of dynamic melting of primitive mantle material (with 1% porosity) by using the partition coefficients of Adam and Green (2006) and Batanova et al. (2008). (For interpretation of the references to colour in this figure legend, the reader is referred to the web version of this article.)

harzburgite and dunite samples (−2.24 to 2.00) from the Dargai peridotites correlate positively with Cr# values of the spinel (Fig. 13a). This relationship supports the idea that these melts, together with subduction-related fluids and magmas, interacted with the upper mantle rocks of upper mantle in the wedge during their ascent to the surface. However, the Cpx-harzburgite samples are characterized by a narrower range of $fO_2$ (−2.11 to +0.60) and by lower and nearly constant spinel Cr# values, which we attribute to fluid-rock interaction (Aldanmaz et al., 2009).

Most of the Cpx-harzburgite samples and some of the depleted harzburgite samples plot between FMQ and FMQ-1 (Fig. 13b) on the V versus MgO diagram suggested by Lee et al. (2003) and Uysal et al. (2012). However, some of the Cpx-harzburgite samples and most of the depleted harzburgite and dunite samples plot between FMQ and FMQ +1. These data do not overlap with oceanic mantle trends depicted in the same figure and represent lower V values. The $fO_2$ value obtained by using the V content could be significantly lower than the $fO_2$ values determined thermodynamically for the subduction zone peridotites using $Fe^{3+}$ activity (Lee et al., 2003; Uysal et al., 2012). However, in more recent research, $fO_2$ valuations achieved on the basis of V values and mineral chemistry are typically consistent (Fig. 13a and b). These observations and our findings indicate that the Dargai Cpx-harzburgites are the result of low degrees of partial melting (first stage melt extraction) in a mid-oceanic ridge (MOR) setting. The depleted harzburgites and dunites were most likely formed by re-melting (second stage melt extraction) of the Cpx-harzburgites in a SSZ setting, generating boninitic melts.

### 7.3. Melt-peridotite interaction and mantle metasomatism

Cr-spinel grains in the Dargai depleted harzburgite samples have high Cr# values of 38–75 and are characterized by very low $TiO_2$ (0.02–0.07 wt%) contents, suggesting derivation from boninitic melts produced by high-degrees of partial melting. Mantle peridotites containing chromite grains with Cr# > 70 have been produced by very high-degrees of partial melting leaving a residue of dunite. However, a few grains with very high Cr# (>70) also appear in the depleted harzburgites (Fig. 12c and d). This appears to be incompatible with a simple melting model and may reflect later refertilization (Barth et al., 2003; Godard et al., 2008). The occurrence of the Cr-spinel, the existence of high $TiO_2$ (up to 0.18 wt%) in some Cr-spinel grains, and the local presence of interstitial clinopyroxene and Cpx-symplectites support the idea of refertilization (Fig. 2b, e and f).

In the Dargai peridotites chromitites classified as high-Cr varieties (Cr# >60) are typically enclosed by dunite envelopes (Arif and Jan, 2006; González-Jiménez et al., 2011; Lian et al., 2018; Ullah et al., 2020b; Uysal et al., 2015). The abundance of Cpx in the peridotites increases rapidly away from the chromitite bodies, suggesting that they crystallized from second-stage boninitic magma (Feng et al., 2018). The dunite pockets enclosing the chromitite bodies are interpreted as residues produced by incongruent melting of pyroxenes due to the interaction between the boninitic magma and upper mantle peridotites (Dilek and Morishita, 2009; Feng et al., 2018; Morishita et al., 2011). This incongruent melting may have enriched the melts in $SiO_2$, moving them into the field of Cr saturation and triggering crystallization (Lian et al., 2018; Pearce et al., 2000; Ullah et al., 2020a; Wu et al., 2018).

Cr-spinel grains in both the Cpx-harzburgite and depleted harzburgite samples have wide-ranging Cr# values (15–75) and are characterized by low Ti contents ($TiO_2$: 0.06 wt%). These grains resulted from the first stage of melting and refertilization, whereas those precipitated from the second stage (boninitic) have higher Cr# values with a much narrower range (62–81). These also have higher Ti ($TiO_2$: up to 0.11 wt%) (Fig. 12d). The $TiO_2$ contents of the Cr-spinels in the depleted harzburgites and dunites increase toward the chromitite deposits. This pattern is explained by refertilization of the peridotites by the melts from which the chromitites crystallized. (Fig. 12d). The same process can change the Al-rich spinel grains in the harzburgites to more Cr-rich varieties. (González-Jiménez et al., 2011; Ullah et al., 2020b; Uysal et al., 2009). Such reactions can lead to positive correlations between $fO_2$ and Cr# values of the spinels (Fig. 13a), (Pearce et al., 2000; Ullah et al., 2020a; Uysal et al., 2009).

Following the first-stage melting, enrichment of most incompatible elements in some of the Cpx-harzburgite samples took place during melt-rock reaction (Fig. 5c). Relatively low- degree partial melts originating from a deeper level could have enriched the overlying mantle in the observed incompatible elements.

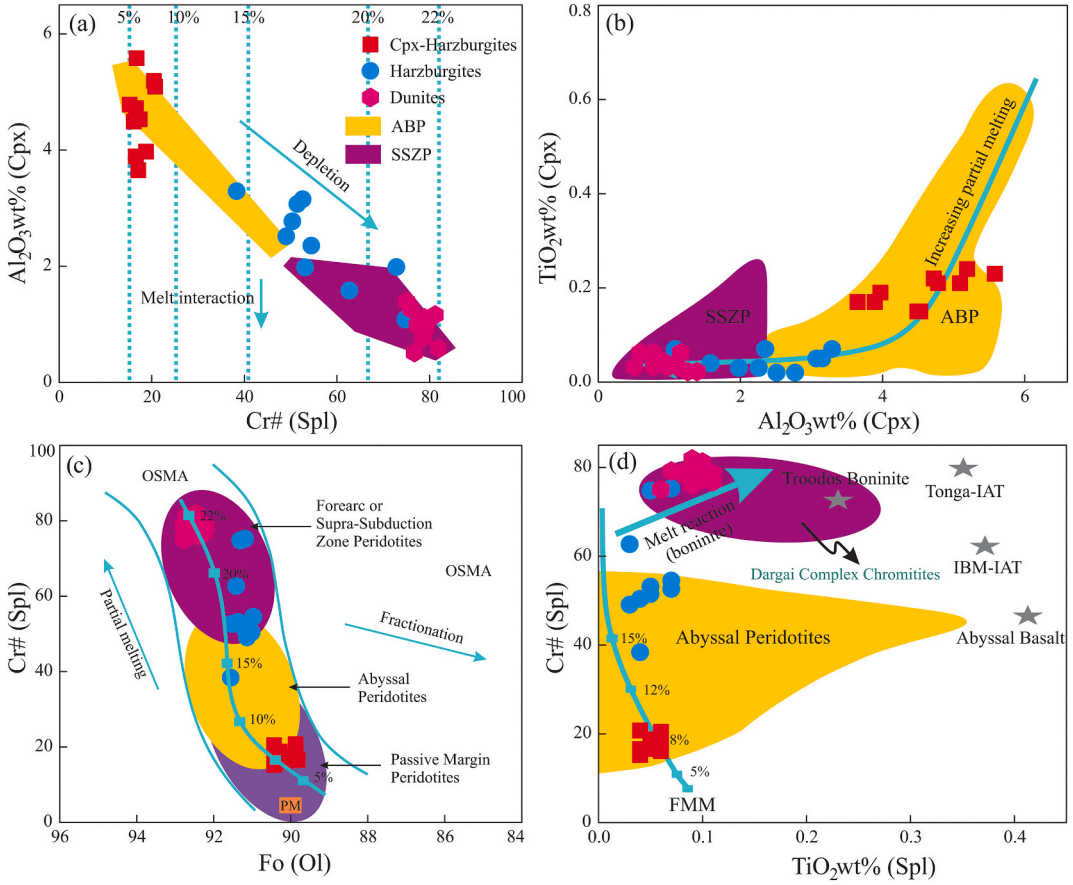


**Fig. 12.** (a) Variation diagrams of $Al_2O_3$ (wt%) contents of clinopyroxene (Cpx) versus Cr# of coexisting Cr-spinel of the Dargai peridotites. The abyssal and SSZ peridotite fields and the trends are from Page and Barnes (2009); (b) $TiO_2$ (wt%) versus $Al_2O_3$ (wt%) contents in clinopyroxene of the Dargai peridotites; (c) Cr# of spinel versus Fo [100 Mg / (Mg + $Fe^{2+}$)] of coexisting olivine from the Dargai peridotites; diagram is from Wu et al. (2018). Passive margin peridotites, ABP, and SSZP fields and the trends are from Lian et al. (2018) and Ullah et al. (2020a). The degrees of melt extraction are calculated on the basis of spinel compositions using the empirical formula of Hellebrand et al. (2001). OSMA-olivine spinel mantle array; (d) Compositional variations of Cr# versus $TiO_2$ (wt%) contents of Cr-spinel in peridotites samples of the Dargai ophiolite. Compositional trends are from Pearce et al. (2000) and the Dargai chromitite field is from Ullah et al. (2020b).

### 7.4. Trace elements

The Dargai depleted harzburgite and dunite samples, which are similar to SSZ peridotites, show notable MREE depletion compared to HREE (Fig. 5d). These samples also show clear enrichment of LREE, LILE, and some HFSE features that are associated with the addition of SSZ slab fluids or melts (Dilek et al., 2007; Dilek and Furnes, 2014; Dilek and Thy, 2009; Parkinson and Pearce, 1998). Similar enrichment of LREE, Sr and Zr has been documented in some boninitic peridotites from the Izu Bonin Mariana forearc environment (Parkinson and Pearce, 1998) (Fig. 5d).

We have modelled melting and enrichment processes in the peridotites using whole-rock and clinopyroxene trace elements to constrain the mode and nature of the petrological processes involved (Tables 5 and 6 and Fig. 14). The weakly depleted Cpx-harzburgites have whole-rock and clinopyroxene mineral chemistry consistent with abyssal-type peridotites formed at mid-oceanic ridges. Thus, we tested a partial melting model of a primitive mantle source for these peridotites (Palme and O'Neill, 2013; Uysal et al., 2012) using Yb versus Ni/Yb systematics to monitor the degree of partial melting, because these elements are less affected by mantle metasomatism or melt-rock interaction than others (Fig. 14a and e). The modelling results support our interpretation that the Cpx-harzburgite samples are the residuals of ~10–15% partial melting of primitive mantle (Fig. 14b and f). Overall, the HREE contents of our samples are consistent with the findings of the REE modelling; again the Cpx-harzburgite have low HREE contents, indicating ~10%–15% partial melting (Fig. 14b and f). The abundances of REE in the Cpx-harzburgite samples are well explained in this model (Fig. 14), and point to a first-stage melting and enrichment in these peridotites.

The depleted harzburgite and dunite samples are clearly more depleted than the Cpx-harzburgites, likely reflecting formation in a SSZ environment. When plotted on the Yb versus Ni/Yb diagram the depleted harzburgites and dunites are consistent with an additional partial melting of the Cpx-harzburgite samples by ~10% and 23% partial melting, respectively (Fig. 14c and e). This interpretation is confirmed by the HREE concentrations of the rocks (Fig. 14d and f). Thus, the trace element data support our interpretation that the depleted harzburgites and dunites record a second-stage melting event in a SSZ environment (c.f., Lian et al., 2018; Ullah et al., 2020a; Wu et al., 2018).

### 7.5. Nature of the mantle source and its control on PGE fractionation

Individual members of the PGE group (Os, Ir, Ru, Rh, Pt, and Pd) in mantle peridotites can fractionate in different way because of their different physiochemical characteristics and melting temperatures (Barnes et al., 2016; Lian et al., 2018; Luguet et al., 2003; Marchesi et al., 2013; Ullah et al., 2020a; Ullah et al., 2020b). The IPGE (Ir-group including Os, Ir and, Ru with melting temperatures >2000°C) mostly occur in discrete minerals or sulfides, commonly as inclusions in silicate or chromite grains, whereas the PPGE (Pd-group PGEs: Rh, Pt, and Pd having melting temperatures <2000°C) are typically enclosed by interstitial sulfides (Alard et al., 2000; Luguet et al., 2007; Ullah et al.,

**Table 8**
Calculation of oxygen fugacities of the Dargai Complex peridotites.

| Lithology | S. No | Spinel Cr# | Spinel Mg# | Spinel $Fe^{3+}/\Sigma Fe$ | Olivine Fo | Temp (K) | $\Delta logfO_2$ (FMQ) | Spinel $Fe^{3+}$ | Spinel $TiO_2$ (wt%) |
|---|---|---|---|---|---|---|---|---|---|
| **Cpx-Harzburgite** | Cpx-H-1 | 18.8 | 72.6 | 0.007 | 90.3 | 894.9 | −2.03 | 0.67 | 0.05 |
| | Cpx-H-2 | 16.1 | 71.3 | 0.007 | 90.2 | 813.5 | −1.76 | 0.56 | 0.06 |
| | Cpx-H-3 | 15.2 | 72.8 | 0.011 | 90.4 | 838.7 | −0.85 | 0.72 | 0.04 |
| | Cpx-H-4 | 17.1 | 71.1 | 0.012 | 90.2 | 836.4 | −0.84 | 0.66 | 0.05 |
| | Cpx-H-5 | 20.5 | 69.8 | 0.033 | 90.4 | 962.5 | 0.39 | 0.73 | 0.06 |
| | Cpx-H-6 | 16.6 | 71.9 | 0.007 | 89.8 | 856.5 | −1.99 | 0.61 | 0.04 |
| | Cpx-H-7 | 16.8 | 72.5 | 0.021 | 90.0 | 953.8 | −0.28 | 0.73 | 0.06 |
| | Cpx-H-8 | 16.6 | 73.8 | 0.006 | 90.4 | 895.5 | −2.11 | 0.41 | 0.05 |
| | Cpx-H-9 | 20.7 | 69.4 | 0.043 | 89.9 | 1036.2 | 0.59 | 0.64 | 0.04 |
| | Cpx-H-10 | 17.4 | 70.7 | 0.016 | 90.2 | 886.9 | −0.53 | 0.56 | 0.06 |
| **Harzburgite** | Hrz-1 | 62.7 | 59.4 | 0.041 | 91.4 | 1102.9 | 0.04 | 0.51 | 0.03 |
| | Hrz-2 | 75.2 | 47.2 | 0.084 | 91.2 | 1086.7 | 1.21 | 0.26 | 0.07 |
| | Hrz-3 | 38.4 | 60.9 | 0.017 | 91.6 | 827.9 | −0.59 | 0.38 | 0.04 |
| | Hrz-4 | 52.6 | 45.6 | 0.040 | 91.5 | 792.8 | 0.72 | 0.85 | 0.07 |
| | Hrz-5 | 74.8 | 50.9 | 0.043 | 91.3 | 1052.6 | 0.11 | 0.88 | 0.05 |
| | Hrz-6 | 49.1 | 55.4 | 0.028 | 91.1 | 863.1 | −0.09 | 0.34 | 0.03 |
| | Hrz-7 | 53.2 | 63.4 | 0.045 | 91.4 | 1120.4 | 0.24 | 0.71 | 0.05 |
| | Hrz-8 | 51.5 | 55.5 | 0.034 | 91.2 | 942.9 | −0.03 | 0.49 | 0.05 |
| | Hrz-9 | 54.5 | 58.8 | 0.040 | 90.9 | 1045.0 | 0.05 | 0.48 | 0.07 |
| | Hrz-10 | 50.4 | 53.9 | 0.009 | 91.0 | 858.1 | −2.23 | 0.21 | 0.04 |
| **Dunite** | Dn-1 | 78.6 | 40.6 | 0.071 | 92.2 | 957.1 | 1.26 | 0.79 | 0.11 |
| | Dn-2 | 75.0 | 40.7 | 0.053 | 92.7 | 897.1 | 0.93 | 0.77 | 0.06 |
| | Dn-3 | 81.9 | 43.2 | 0.088 | 92.5 | 1020.5 | 1.65 | 1.12 | 0.09 |
| | Dn-4 | 81.2 | 38.9 | 0.098 | 92.7 | 965.9 | 1.94 | 0.91 | 0.10 |
| | Dn-5 | 76.8 | 42.3 | 0.051 | 92.3 | 935.9 | 0.73 | 1.29 | 0.11 |
| | Dn-6 | 79.2 | 40.1 | 0.079 | 92.4 | 1481.0 | 1.96 | 0.74 | 0.07 |
| | Dn-7 | 78.9 | 43.9 | 0.062 | 92.8 | 1426.1 | 1.61 | 0.97 | 0.09 |
| | Dn-8 | 77.3 | 37.7 | 0.074 | 92.8 | 1456.9 | 2.00 | 0.77 | 0.10 |
| | Dn-9 | 78.7 | 37.4 | 0.061 | 92.6 | 1466.3 | 1.63 | 0.85 | 0.08 |
| | Dn-10 | 75.9 | 41.1 | 0.045 | 92.4 | 1301.7 | 0.99 | 0.88 | 0.09 |

*Note:* Formula units based on 32 oxygens and $Fe^{2+}/Fe^{3+}$ assuming full site occupancy. Cr# =100*Cr/(Cr + Al); Mg# = 100*Mg/(Mg + $Fe^{2+}$); $Fe^{3+}$# = 100 $Fe^{3+}$/($Fe^{3+}$ + Cr + Al). Temp-temperature; FMQ-fayalite-magnetite-quartz buffer.

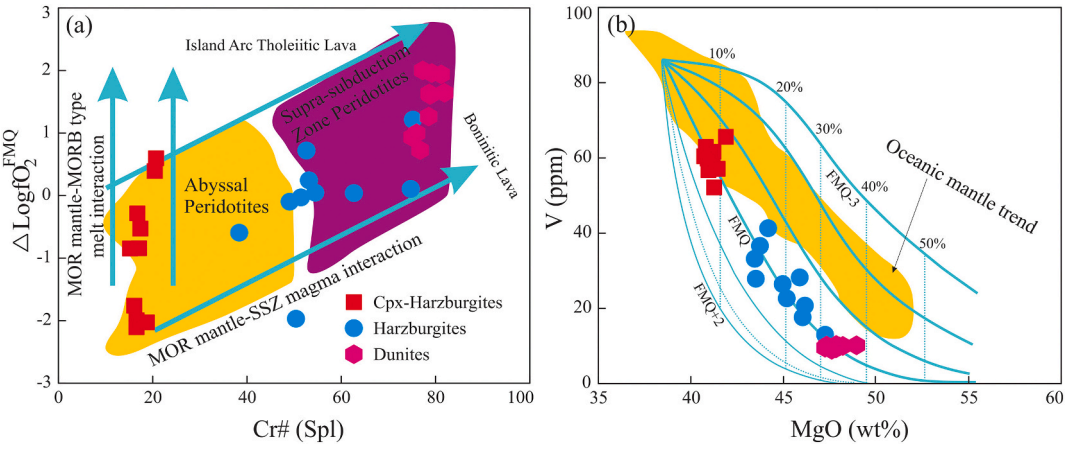


**Fig. 13.** (a) Plot of $\Delta logfO_2$ (FMQ-fayalite-magnetite-quartz buffer) versus Cr# of Cr-spinels from the Dargai Cpx-harzburgites, depleted harzburgites and dunites. Abyssal and SSZ peridotite (Parkinson and Pearce, 1998) discrimination boundaries are shown for comparison; (b) modelling of melting degrees and oxygen fugacities of the Dargai peridotites using the covariation of V-MgO (after Lee et al., 2003). Partial melting curves are at 1 log unit intervals, spanning $fO_2$ from FMQ −3 to FMQ +2 (thick solid line represents FMQ). The unbuffered fractional melting is represented by a dashed line in which $fO_2$ is initially arranged to be FMQ but allowed to change with progressive melting in a system closed to $O_2$ exchange. Vertical dotted lines show the degree of melt extraction in 10% increments (Lee et al., 2003). Oceanic mantle field data are from Bodinier (1988) and Burnham et al. (1998).

2020a, 2020b; Wu et al., 2018). Variations in PGE geochemistry in the Dargai peridotites provide some guidelines to the partial melting and melting processes by which these rocks formed. For examples, all of the PGEs are relatively incompatible in upper mantle peridotites with the incompatibilities decreasing from Os to Pd, Pt, and Pd. Therefore, apparent enrichment of Os and Ir in the mantle residue is actually due to in the relative depletion of Pt and Pd during partial melting (Brenan et al., 2003). In addition, all the PGEs are strongly compatible in sulfides thus, the presence of sulfide phases at various stages of mantle melting has a significant impact on PGE abundances in both the melts and the residual peridotites (Barnes et al., 1997; Bockrath et al., 2004; Brenan et al., 2003; Zhou et al., 2005).

Marchesi et al. (2013) modelled a diagrammatic representation of PGE behaviors against $Al_2O_3$ values during partial melting of primitive upper mantle by using values from McDonough and Sun (1995) (Fig. 10). Theoretically calculated depletion trends are also shown on the same diagram (Marchesi et al., 2013). The Dargai Cpx-harzburgite samples are mostly depleted by ~10%–15% compared to the primitive upper mantle, but their Pd values are much higher than those predicted by the modelled $Al_2O_3$ trend (Fig. 10f). We suggest that the Pd

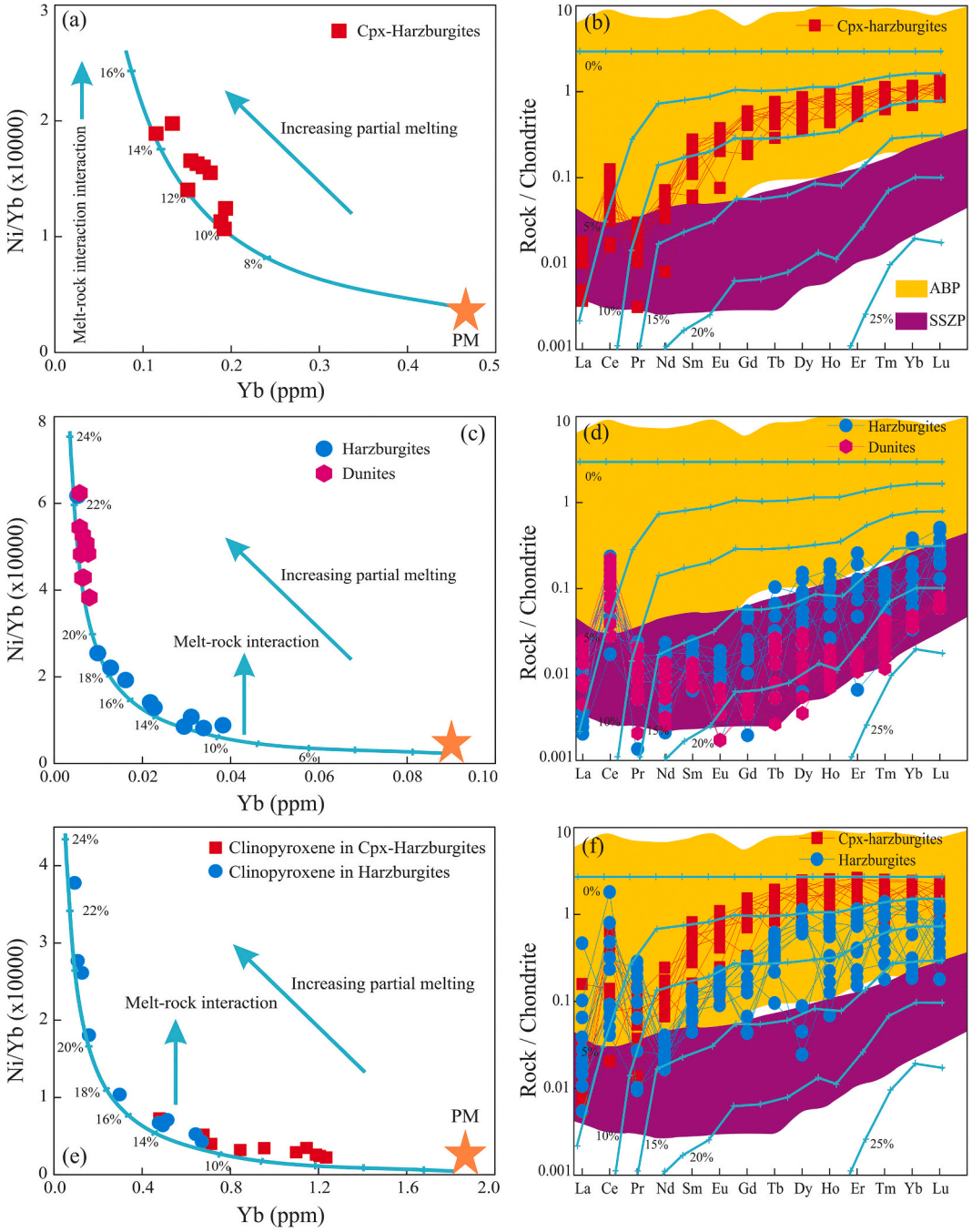


**Fig. 14.** Trace elements patterns of the representative peridotite, Cpx in Cpx-harzburgite and depleted harzburgite samples for the Dargai ophiolite (Chondrite-normalized values are from Palme and O'Neill, 2013); (a) variation diagram of Ni/Yb versus Yb (ppm); (b) chondrite-normalized trace elements pattern for representative Cpx-harzburgite samples; (c) variation diagram of Ni/Yb versus Yb (ppm); (d) chondrite-normalized trace elements pattern for representative harzburgite and dunite samples; (e) Ni/Yb versus Yb (ppm) bivariate diagram; (f) chondrite-normalized trace elements patterns for representative Cpx-harzburgite and harzburgite samples. Abyssal peridotite data are taken from Niu et al. (1997). Supra-subduction zone peridotite data are from Parkinson and Pearce (1998).

enrichment reflects melt-mantle interaction in a MOR setting. According to their REE compositions, the Dargai depleted harzburgites and dunites underwent ~20%–35% total partial melting, respectively, much higher than suggested by their $Al_2O_3$ contents. We interpret the difference as the result of very high degrees of partial melting and/or extensive melt-rock reaction this time in a SSZ environment. Late stage, hydrous melts in SSZ environments involve very high degrees of partial melting, perhaps sufficient to enrich the magmas in normally incompatible PGEs (particularly Os, Ir and Ru). Later interaction between these melts and the overlying mantle could significantly enrich the remaining peridotites (Fig. 10). Thus, the PGE compositions alone cannot reliably measure of the degree of partial melting. Our analyzed samples show a slightly positive trend from Os to Pd (Fig. 9), which is unusual in residual mantle material and suggests at least some degree of enrichment by melt/rock reaction (Alard et al., 2000; Barnes et al., 1997; Brenan et al., 2003; Lian et al., 2018; Ullah et al., 2020a, 2020b).

### 7.6. *Re-Os constraints on provenance and mantle processes*

The high values of Re of the samples (up to 1.92 ppb) compared to the primitive mantle (0.28 ppb); Meisel et al., 2001) cannot be explained by simple melt extraction, suggesting some degree of secondary Re

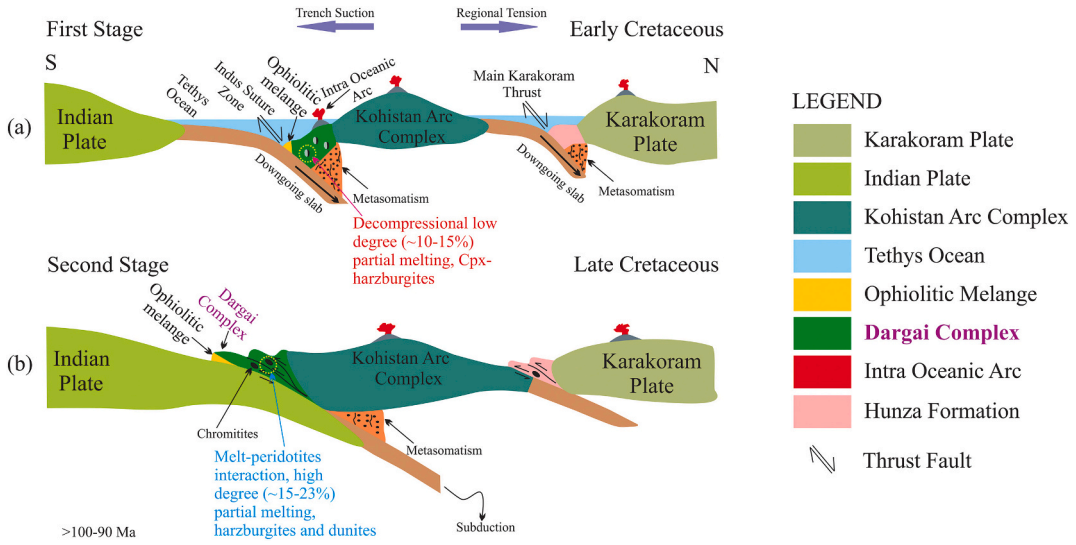


**Fig. 15.** Tectonic model for the two stages of melt evolution of the Cpx-harzburgite, depleted harzburgite and dunite-chromitites occurrences in the Dargai Ophiolite along the Main Mantle Thrust (MMT or Indus Suture Zone), North Pakistan (modified after Burg et al., 1998; Schaltegger et al., 2002). See text for discussion.

addition. Metamorphism, ophiolite emplacement, partial melting, seafloor metamorphism, and serpentinization are considered to be effective processes for mobilizing Re in oceanic crust and lithosphere (c.f., Batanova et al., 2008; Feng et al., 2018; Uysal et al., 2012). Thus, the most ancient processes triggering mobilization of Re should not be older than ca. 250 Ma, which represents the time at which Neo-Tethys opened (Batanova et al., 2008; Feng et al., 2018; Feng et al., 2021; Uysal et al., 2012). However, the Re vs $Al_2O_3$ diagram (Fig. 11a) suggests that Re could have been added to the Dargai peridotites any time after mid-ocean spreading ceased at ca. 250 Ma (Feng et al., 2018, Feng et al., 2021, Uysal et al., 2012). Therefore, we recalculated the likely original concentrations of Re in our samples using the technique reported by Batanova et al. (2008). Using these recalculated concentrations of Re, and the minimum $T_{RD}$ and $T_{MA}$ proposed by Batanova et al. (2008) and Uysal et al. (2012) for Tethyan ophiolites, we have identified a sequence of possible depletion processes linked to the opening of the Neo-Tethys, Rheic, and Proto-Tethys Oceans, between ca. 250 ma and ca.450 Ma. The older >1000 Ma old ages related to previous depletion processes prior to the opening of Proto-Tethys could plausibly be linked to melting processes in Gondwana's sub-continental lithospheric mantle. As a result, we conclude that our samples conceivably preserve a record of a heterogeneous upper mantle that has been subjected to several ancient depletion events.

In summary, we propose that the Dargai peridotites were formed by two stages of partial melting and melt-rock reaction in two different tectonic environments. Initially, the Cpx-harzburgites were produced by low degrees of partial melting at a mid-ocean ridge; during this stage the percolating melts also segregated their sulfides and transferred the mantle's $^{187}Os/^{188}Os$ signature to the rocks. The depleted harzburgites and dunites were formed later by much higher degrees of partial melting of the Cpx-harzburgite in an SSZ environment. We further suggest that both partial melting processes and associated melt-rock interactions may have occurred in a trench-distal forearc basin spreading center with variable subduction effects (Arif and Jan, 2006; Jan and Howie, 1981; Ullah et al., 2020a; Ullah et al., 2020b). This interpretation is consistent with geodynamic models that propose a northern regional progression of tectonic and magmatic processes in the northern Pakistan Neo-Tethyan ophiolites (Arif and Jan, 2006; Jan and Howie, 1981; Ullah et al., 2020a; Ullah et al., 2020b).

### 7.7. A possible petrogenetic model and regional implications

The Kohistan Arc Complex (KAC) in northern Pakistan is an exhumed, early Cretaceous intra-oceanic arc unit that was formed during northward subduction of Neo-Tethyan lithosphere beneath the Karakorum Plate (Burg et al., 1998; Faisal et al., 2014; Faisal et al., 2016; Schaltegger et al., 2002). This complex is presently wedged between the Indian plate to the south and the Karakoram (Asian) plate to the north. and is separated from these blocks by the Main Mantle Thrust to the north (MMT) and the main Kohistan thrust (MKT) to the south. The Dargai Complex, is currently emplaced on the hanging wall of the MMT, exposing the ultramafic roots of the KAC, which was formed at ca. 110–90 Ma (Burg et al., 1998; Faisal et al., 2014; Faisal et al., 2016; Schaltegger et al., 2002).

Here we present a tectono-magmatic model for the Dargai Complex peridotites based on field observations and geochemical data, which calls for at least two stages of melt depletion and refertilization, to constrain the tectonic setting of the Indus Suture Zone ophiolites (Fig. 15). The first phase (Fig. 15a) was characterized by upwelling of asthenosphere below a spreading ridge that generated MORB-like melts and a residue of Cpx-harzburgite. In the second phase (Fig. 15b), remelting of the Cpx-harzburgites yielded depleted harzburgites, dunites, and boninitic melts. In both cases, the residual peridotites and dunites were modified by infiltration of the related melts.

Trace element abundances of the Cpx-harzburgite samples formed during stage one suggest ~10%–15% partial melting of a chondrite-normalized mantle source (Fig. 15a), whereas stage-two melts were formed by ~15%–23% additional melting of the Cpx-harzburgites. Theoretically, the trace element compositions of the depleted harzburgite and dunite samples could also have been generated by partial melting of an already depleted mantle (Fig. 15b).

Our PGE data also support these melting models. Chondrite-normalized PGE patterns of the analyzed samples do not show an expected negative slope from Os to Pd for partial melting residuals. This infers that the PGEs, particularly the most incompatible ones, were redistributed during melting along the mantle wedge. Widely ranging Re depletion ages of the samples are most likely related to tectonic activities associated with opening and closure of Neo-Tethys. For example: (1) opening of Neo-Tethys by seafloor spreading (ca. 250 Ma), and (2) closing of Neo-Tethys via intra-oceanic subduction (ca. 90 Ma). The Re abundances of the primitive mantle were depleted at ca. 250 Ma during the first stage of depletion. Before the second melting stage at ca. 90 Ma,

the residual values of $^{187}Re$ in the restite decayed into $^{187}Os$. Any remaining $^{187}Re$ contents would have decayed to $^{187}Os$ during the second melting event. This explains why the $^{187}Os/^{188}Os$ values of the Cpx-harzburgites that formed during the first stage of melting are so much higher those of the depleted harzburgite residue of the second stage. The model ages of the Dargai peridotites, the model ages between ca. 250 Ma and ca. 450 Ma may be related to tectonic events, linked to the geodynamic evolution of the Neo-Tethys, Rheic, and Proto-Tethyan Oceans (Feng et al., 2018, Feng et al., 2021, Uysal et al., 2012). The >1000 Ma model ages that we identified are thought to be related to an older melting event that preceded the opening of Proto-Tethys. Future, more detailed investigations of the Re-Os isotope systematics of the Dargai peridotites should provide critical information on the distribution, composition, and genesis of the mantle rocks beneath the Indus Suture Zone and the northern limb of the Kohistan Arc Complex.

## 8. Conclusions

On the basis of field observations, petrography, mineralogy, whole-rock geochemistry, and isotopic data, we conclude that the Cpx-harzburgites, depleted harzburgites, and dunites of the Dargai Complex reveal two stages of partial melting and refertilization during the evolution of the Neo-Tethyan mantle in this region. The Cpx-harzburgites produced by the first stage, show low degrees of partial melting (~10%–15%) prior to their modification by melt percolation processes beneath a seafloor spreading center. In contrast, the depleted harzburgites and dunites are considered to be products of an additional ~15%–23% partial melting, respectively, of the Cpx peridotites.

The high degrees of the second-stage melting are thought to have produced boninitic melts, some of which interacted with, and re-fertilized, the residual peridotites and dunites with PGEs and changed the *Re*-Os systematics. The percolating melts segregated the mantle sulfides and gave these depleted rocks a melt like signature of $^{187}Os/^{188}Os$. The Neo-Tethyan mantle had a strongly heterogeneous Os isotopic compositions compared to upper mantle peridotites in the two sub-belts of the Dargai Complex in the Indus Suture Zone.

## Declaration of Competing Interest

The authors declared that there is no conflict of interest.

## Acknowledgements

This research was financially supported by a grant from the Science and Technology Innovation Program of Hunan Province (Grant No. 2021RC4055), and Key Laboratory of Metallogenic Prediction of Nonferrous Metals and Geological Environment Monitoring, during the Postdoctoral research of the first author at the Central South University, Changsha, China. We are grateful to Prof. Dr. Michael W. Förster (DEES, Macquarie University, Australia) for correcting grammatical and syntax errors in the manuscript. We thank the Editor-in-Chief, Managing Guest Editor Prof. Dr. Paul T. Robinson, and two anonymous reviewers for their useful comments and suggestions which helped to improve the quality and presentation of the manuscript.

## References

Adam, J., Green, T., 2006. Trace element partitioning between mica- and amphibole-bearing garnet lherzolite and hydrous basanitic melt: 1. Experimental results and the investigation of controls on partitioning behaviour. Contrib. Mineral. Petrol. 152, 1–17.

Ahmed, Z., 1982. Porphyritic-nodular, nodular, and orbicular chrome ores from the Sakhakot-Qila complex Pakistan, and their chemical variations. Mineral. Mag. 45, 167–178.

Ahmed, Z., 1984. Stratigraphic and textural variations in the chromite composition of the ophiolitic Sakhakot-Qila complex, Pakistan. Econ. Geol. 79, 1334–1359.

Alard, O., Griffin, W.L., Lorand, J-P., Jackson, S.E., O'Reilly, S.Y., 2000. Non-chondritic distribution of the highly siderophile elements in mantle sulphides. Nature 407, 891–894.

Aldanmaz, E., Schmidt, M.W., Gourgaud, A., Meisel, T., 2009. Mid-ocean ridge and supra-subduction geochemical signatures in spinel-peridotites from the Neotethyan ophiolites in SW Turkey: implications for upper mantle melting processes. Lithos 113, 691–708.

Arai, S., 1992. Chemistry of chromian spinel in volcanic rocks as a potential guide to magma chemistry. Mineral. Mag. 56, 173–184.

Arculus, R.J., 1994. Aspects of magma genesis in arcs. Lithos 33, 189–208.

Arif, M., Jan, M.Q., 2006. Petrotectonic significance of the chemistry of chromite in the ultramafic-mafic complexes of Pakistan. J. Asian Earth Sci. 27, 628–646.

Ballhaus, C., 1998. Origin of podiform chromite deposits by magma mingling. Earth Planet. Sci. Lett. 156, 185–193.

Ballhaus, C., Berry, R.F., Green, D.H., 1991. High pressure experimental calibration of the olivine-orthopyroxene-spinel oxygen geobarometer: implications for the oxidation state of the upper mantle. Contrib. Mineral. Petrol. 107, 27–40.

Barnes, S.J., Lightfoot, P.C., 2005. Formation of magmatic nickel-sulfide ore deposits and processses affecting their copper and platinum-group element contents. In: Hedenquist, J.W., Thompson, J.F.H., Goldfarb, R.J., Richards, J.P. (Eds.), Economic Geology 100th Anniv., pp. 179–213.

Barnes, S.J., Makovicky, E., Makovicky, M., Rose-Hansen, J., Karup-Moller, S., 1997. Partition coefficients for Ni, Cu, Pd, Pt, Rh, and Ir between monosulfide solid solution and sulfide liquid and the formation of compositionally zoned Ni-Cu sulfide bodies by fractional crystallization of sulfide liquid. Can. J. Earth Sci. 34, 366–374.

Barnes, S.J., Pagé, P., Prichard, H.M., Zientek, M.L., Fisher, P.C., 2016. Chalcophile and platinum-group element distribution in the Ultramafic series of the Stillwater Complex, MT, USA—implications for processes enriching chromite layers in Os, Ir, Ru, and Rh. Mineral. Deposita 51, 25–47.

Barth, M.G., Mason, P.R.D., Davies, G.R., Dijkstra, A.H., Drury, M.R., 2003. Geochemistry of the Othris Ophiolite, Greece: evidence for refertilization? J. Petrol. 44, 1759–1785.

Batanova, V.G., Brügmann, G.E., Bazylev, B.A., Sobolev, A.V., Kamenetsky, V.S., Hofmann, A.W., 2008. Platinum-group element abundances and Os isotope composition of mantle peridotites from the Mamonia complex, Cyprus. Chem. Geol. 248, 195–212.

Bockrath, C., Ballhaus, C., Holzheid, A., 2004. Stabilities of laurite RuS2 and monosulfide liquid solution at magmatic temperature. Chem. Geol. 208, 265–271.

Bodinier, J.L., 1988. Geochemistry and petrogenesis of the Lanzo peridotite body, western Alps. Tectonophysics 149, 67–88.

Brenan, J.M., McDonough, W.F., Dalpé, C., 2003. Experimental constraints on the partitioning of rhenium and some platinum-group elements between olivine and silicate melt. Earth Planet. Sci. Lett. 212, 135–150.

Burg, J.P., Bodinier, J.L., Chaudhry, S., Hussain, S., Dawood, H., 1998. Infra-arc mantle-crust transition and intra-arc mantle diapirs in the Kohistan complex (Pakistani Himalaya): petro-structural evidence. Terra Nova 10, 74–80.

Burnham, O.M., Rogers, N.W., Pearson, D.G., Van Calsteren, P.W., Hawkesworth, C.J., 1998. The petrogenesis of the eastern Pyrenean peridotites: an integrated study of their whole-rock geochemistry and Re-Os isotope composition. Geochim. Cosmochim. Acta 62, 2293–2310.

Dai, J.G., Wang, C.S., Hébert, R., Santosh, M., Li, Y.L., Xu, J.Y., 2011. Petrology and geochemistry of peridotites in the Zhongba ophiolite, Yarlung Zangbo Suture Zone: Implications for the early cretaceous intra-oceanic subduction zone within the Neo-Tethys. Chem. Geol. 288, 133–148.

Dick, H.J.B., Natland, J.H., 1996. Late-Stage Melt Evolution and Transport in the Shallow Mantle Beneath the East Pacific Rise. Deep see Drilling Project, Initial Report 147, pp. 103–134.

Dilek, Y., Furnes, H., 2011. Ophiolite genesis and global tectonics: geochemical and tectonic fingerprinting of ancient oceanic lithosphere. Geol. Soc. Am. Bull. 123, 387–411.

Dilek, Y., Furnes, H., 2014. Ophiolites and their origins. Elements 10, 93–100.

Dilek, Y., Furnes, H., 2018. Tethyan ophiolites and tethyan seaways. J. Geol. Soc. Lond. 176, 899–912.

Dilek, Y., Morishita, T., 2009. Melt migration and upper mantle evolution during incipient arc construction: Jurassic Eastern Mirdita ophiolite, Albania. Island Arc 18, 551–554.

Dilek, Y., Thy, P., 2009. Island arc tholeiite to boninitic melt evolution of the cretaceous Kizildag (Turkey) ophiolite: model for multi-stage early arc-forearc magmatism in Tethyan subduction factories. Lithos 113, 68–87.

Dilek, Y., Furnes, H., Shallo, M., 2007. Suprasubduction zone ophiolite formation along the periphery of Mesozoic Gondwana. Gondwana Res. 11, 453–475.

Dipietro, J.A., Hussain, A., Ahmad, I., Khan, M.A., 2000. The main mantle thrust in Pakistan: its character and extent. Geol. Soc. Lond. Spec. Publ. 170, 375–393.

Faisal, S., Larson, K.P., Cottle, J.M., Lamming, J., 2014. Building the Hindu Kush: monazite records of terrane accretion, plutonism and the evolution of the Himalaya-Karakoram-Tibet orogen. Terra Nova 26, 395–401.

Faisal, S., Larson, K.P., King, J., Cottle, J.M., 2016. Rifting, subduction and collisional records from pluton petrogenesis and geochronology in the Hindu Kush, NW Pakistan. Gondwana Res. 35, 286–304.

Feng, G., Yang, J., Dilek, Y., Liu, F., Xiong, F., 2018. Petrological and Re-Os isotopic constraints on the origin and tectonic setting of the Cuobuzha peridotite, Yarlung Zangbo suture zone, southwest Tibet, China. Lithosphere 10, 95–108.

Feng, G., Yang, J., Niu, X., Liu, F., Qiu, T., Dilek, Y., 2021. Formation processes and tectonic implications of mantle peridotites of the Yushigou ophiolite in the North Qilian Orogenic Belt, NW China. Lithos 400–401.

Gaetani, G.A., Grove, T.L., 1998. The influence of water on melting of mantle peridotite. Contrib. Mineral. Petrol. 131, 323–346.
Gao, S., Ling, W., Qiu, Y., Lian, Z., Hartmann, G., Simon, K., 1999. Contrasting geochemical and Sm-Nd isotopic compositions of Archean metasediments from the Kongling high-grade terrain of the Yangtze craton: evidence for cratonic evolution and redistribution of REE during crustal anatexis. Geochim. Cosmochim. Acta 63, 2071–2088.
Garuti, G., Fershtater, G., Bea, F., Montero, P., Pushkarev, E.V., Zaccarini, F., 1997. Platinum-group elements as petrological indicators in mafic-ultramafic complexes of the central and southern Urals: preliminary results. Tectonophysics 276, 181–194.
Godard, M., Lagabrielle, Y., Alard, O., Harvey, J., 2008. Geochemistry of the highly depleted peridotites drilled at ODP Sites 1272 and 1274 (Fifteen-Twenty Fracture Zone, Mid-Atlantic Ridge): implications for mantle dynamics beneath a slow spreading ridge. Earth Planet. Sci. Lett. 267, 410–425.
González-Jiménez, J.M., Proenza, J.A., Gervilla, F., Melgarejo, J.C., Blanco-Moreno, J.A., Ruiz-Sánchez, R., Griffin, W.L., 2011. High-Cr and high-Al chromitites from the Sagua de Tánamo district, Mayarí-Cristal ophiolitic massif (eastern Cuba): Constraints on their origin from mineralogy and geochemistry of chromian spinel and platinum-group elements. Lithos 125, 101–121.
Hellebrand, E., Snow, J.E., Dick, H.J.B., Hofmann, A.W., 2001. Coupled major and trace elements as indicators of the extent of melting in mid-ocean-ridge peridotites. Nature 410, 677–681.
Jackson, S.E., Fryer, B.J., Gosse, W., Healey, D.C., Longerich, H.P., Strong, D.F., 1990. Determination of the precious metals in geological materials by inductively coupled plasma-mass spectrometry (ICP-MS) with nickel sulphide fire-assay collection and tellurium coprecipitation. Chem. Geol. 83 (1–2), 119–132.
Jan, M.Q., Howie, R.A., 1981. The mineralogy and geochemistry of the metamorphosed basic and ultrabasic rocks of the jijal complex, Kohistan, NW Pakistan. J. Petrol. 22, 85–126.
Kakar, M.I., Kerr, A.C., Mahmood, K., Collins, A.S., Khan, M., McDonald, I., 2014. Supra-subduction zone tectonic setting of the Muslim Bagh Ophiolite, northwestern Pakistan: Insights from geochemistry and petrology. Lithos 202–203, 190–206.
Khedr, M.Z., Arai, S., Python, M., Tamura, A., 2014. Chemical variations of abyssal peridotites in the central Oman ophiolite: evidence of oceanic mantle heterogeneity. Gondwana Res. 25, 1242–1262.
Lapierre, H., Samper, A., Bosch, D., Maury, R.C., Béchennec, F., Cotten, J., Demant, A., Brunet, P., Keller, F., Marcoux, J., 2004. The Tethyan plume: geochemical diversity of Middle Permian basalts from the Oman rifted margin. Lithos 74, 167–198.
Lee, C.T.A., Brandon, A.D., Norman, M., 2003. Vanadium in peridotites as a proxy for paleo-fO2 during partial melting: prospects, limitations, and implications. Geochim. Cosmochim. Acta 67, 3045–3064.
Li, J., Jiang, X.Y., Xu, J.F., Zhong, L.F., Wang, X.C., Wang, G.Q., Zhao, P.P., 2014. Determination of platinum-group elements and Re-Os isotopes using ID-ICP-MS and N-TIMS from a single digestion after two-stage column separation. Geostand. Geoanal. Res. 38, 37–50.
Li, J., Zhao, P.P., Liu, J., Wang, X.C., Yang, A.Y., Wang, G.Q., Xu, J.F., 2015. Reassessment of hydrofluoric acid desilicification in the carius tube digestion technique for Re-Os isotopic determination in geological samples. Geostand. Geoanal. Res. 39, 17–30.
Lian, D., Yang, J., Dilek, Y., Rocholl, A., 2018. Mineralogy and geochemistry of peridotites and chromitites in the aladag ophiolite (Southern Turkey): melt evolution of the cretaceous neotethyan mantle. J. Geol. Soc. Lond. 176, 958–974.
Liang, Q., Jing, H., Gregoire, D.C., 2000. Determination of trace elements in granites by inductively coupled plasma mass spectrometry. Talanta 51, 507–513.
Lorand, J.P., Alard, O., Luguet, A., 2010. Platinum-group element micronuggets and refertilization process in Lherz orogenic peridotite (northeastern Pyrenees, France). Earth Planet. Sci. Lett. 289, 298–310.
Luguet, A., Lorand, J.P., Seyler, M., 2003. Sulfide petrology and highly siderophile element geochemistry of abyssal peridotites: a coupled study of samples from the Kane Fracture Zone (45°W 23°20N, MARK area, Atlantic Ocean). Geochim. Cosmochim. Acta 67, 1553–1570.
Luguet, A., Shirey, S.B., Lorand, J.P., Horan, M.F., Carlson, R.W., 2007. Residual platinum-group minerals from highly depleted harzburgites of the Lherz massif (France) and their role in HSE fractionation of the mantle. Geochim. Cosmochim. Acta 71, 3082–3097.
Mahmood, K., Boudier, F., Gnos, E., Monié, P., Nicolas, A., 1995. 40Ar/39Ar dating of the emplacement of the Muslim Bagh ophiolite, Pakistan. Tectonophysics 250, 169–181.
Marchesi, C., Garrido, C.J., Harvey, J., González-Jiménez, J.M., Hidas, K., Lorand, J.P., Gervilla, F., 2013. Platinum-group elements, S, Se and Cu in highly depleted abyssal peridotites from the Mid-Atlantic Ocean Ridge (ODP Hole 1274A): influence of hydrothermal and magmatic processes. Contrib. Mineral. Petrol. 166, 1521–1538.
Matsumoto, I., Arai, S., 2001. Morphological and chemical variations of chromian spinel in dunite-harzburgite complexes from the Sangun zone (SW Japan): implications for mantle/melt reaction and chromitite formation processes. Mineral. Petrol. 73, 305–323.
McDonough, W.F., Sun, S.S., 1995. The composition of the Earth. Chem. Geol. 120, 223–253.
Meisel, T., Moser, J., Wegscheider, W., 2001. Recognizing heterogeneous distribution of platinum group elements (PGE) in geological materials by means of the Re-Os isotope system. Fresenius J. Anal. Chem. 370, 566–572.
Moghadam, H.S., Corfu, F., Stern, R.J., 2013. U-pb zircon ages of late cretaceous Nain-dehshir ophiolites, central Iran. J. Geol. Soc. Lond. 170, 175–184.
Morishita, T., Dilek, Y., Shallo, M., Tamura, A., Arai, S., 2011. Insight into the uppermost mantle section of a maturing arc: the Eastern Mirdita ophiolite, Albania. Lithos 124, 215–226.
Niu, Y., 2004. Bulk-rock major and trace element compositions of abyssal peridotites: Implications for mantle melting, melt extraction and post-melting processes beneath Mid-Ocean ridges. J. Petrol. 45, 2423–2458.
Niu, Y., Langmuir, C.H., Kinzler, R.J., 1997. The origin of abyssal peridotites: a new perspective. Earth Planet. Sci. Lett. 152, 251–265.
Niu, X.L., Yang, J.S., Chen, S.Y., Liu, F., Xiong, F.H., Liu, Z., Guo, G.L., 2013. The reformation of the Dongbo ultramafic rock massif in the western part of the Yarlung Zangbo suture zone by subduction-related fluids: evidence from the platimun-group elements (PGE). Geol. China 40, 756–766.
Page, P., Barnes, S.-J., 2009. Using trace elements in chromites to constrain the origin of podiform chromitites in the Thetford Mines Ophiolite, Quebec, Canada. Econ. Geol. 104, 997–1018.
Palme, H., O'Neill, H., 2013. Cosmochemical estimates of mantle composition. In: Holland, H.D., Turrekian, K.K. (Eds.), Treatise on Geochemistry, Second vol. 2. Elsevier, Amsterdam, pp. 1–39.
Parkinson, I.J., Arculus, R.J., 1999. The redox state of subduction zones: Insights from arc-peridotites. Chem. Geol. 160, 409–423.
Parkinson, I.J., Pearce, J.A., 1998. Peridotites from the Izu-Bonin-Mariana forearc (ODP Leg 125): evidence for mantle melting and melt-mantle interaction in a supra-subduction zone setting. J. Petrol. 39, 1577–1618.
Pearce, J.A., Barker, P.F., Edwards, S.J., Parkinson, I.J., Leat, P.T., 2000. Geochemistry and tectonic significance of peridotites from the South Sandwich arc-basin system, South Atlantic. Contrib. Mineral. Petrol. 139, 36–53.
Potts, P.J., Kane, J.S., 2005. International association of geoanalysts certificate of analysis: certified reference material OU-6 (Penrhyn Slate). Geostand. Geoanal. Res. 29, 233–236.
Prichard, H.M., Neary, C.R., Fisher, P.C., O'Hara, M.J., 2008. PGE-rich podiform chromitites in the Al 'Ays ophiolite complex, Saudi Arabia: an example of critical mantle melting to extract and concentrate PGE. Econ. Geol. 103, 1507–1529.
Robinson, P.T., Zhou, M.F., Malpas, J., Bai, W.J., 1997. Podiform chromitites: their composition, origin and environment of formation. Episodes 20, 247–252.
Saccani, E., Tassinari, R., 2015. The role of morb and ssz magma-types in the formation of jurassic ultramafic cumulates in the mirdita ophiolites (Albania) as deduced from chromian spinel and olivine chemistry. Ofioliti 40, 37–56.
Saccani, E., Dilek, Y., Photiades, A., 2018. Time-progressive mantle-melt evolution and magma production in a Tethyan marginal sea: a case study of the Albanide-Hellenide ophiolites. Lithosphere 10, 35–53.
Saka, S., Uysal, I., Akmaz, R.M., Kaliwoda, M., Hochleitner, R., 2014. The effects of partial melting, melt-mantle interaction and fractionation on ophiolite generation: constraints from the late cretaceous Pozanti-Karsanti ophiolite, southern Turkey. Lithos 202–203, 300–316.
Schaltegger, U., Zeilinger, G., Frank, M., Burg, J.P., 2002. Multiple mantle sources during island arc magmatism: U-Pb and Hf isotopic evidence from the Kohistan arc complex, Pakistan. Terra Nova 14, 461–468.
Shallo, M., Dilek, Y., 2003. Development of the Ideas on the Origin of Albanian Ophiolites. Spec. Pap. Geological Society of America 373, pp. 351–363.
Shirey, S.B., Walker, R.J., 1998. The Re–Os isotope system in cosmochemistry and hightemperature geochemistry. Annu. Rev. Earth Planet. Sci. 26, 423–500.
Smoliar, M.I., Walker, R.J., Morgan, J.W., 1996. Re–Os ages of Groups IIA, IIIA, IVA, and IVB iron meteorites. Science 271, 1099–1102.
Snow, J.E., Dick, H.J.B., 1995. Pervasive magnesium loss by marine weathering of peridotite. Geochim. Cosmochim. Acta 59, 4219–4235.
Sun, Y., Sun, M., 2005. Nickel sulfide fire assay improved for pre-concentration of platinum group elements in geological samples: a practical means of ultra-trace analysis combined with inductively coupled plasma-mass spectrometry. Analyst 130, 664–669.
Thompson, M., Potts, P.J., Kane, J.S., Webb, P.C., Watson, J.S., 2000. GeoPT4. An international proficiency test for analytical geochemistry laboratories - report on round 4 (March 1999). Geostand. Geoanal. Res. 24, E1–E37.
Ullah, Z., Li, J.W., Robinson, P.T., Wu, W.W., Khan, A., Dac, N.X., Adam, M.M.A., 2020a. Mineralogy and geochemistry of peridotites and chromitites in the Jijal complex ophiolite along the Main Mantle Thrust (MMT or Indus Suture Zone) North Pakistan. Lithos 366, 105566.
Ullah, Z., Shah, M.T., Siddiqui, R.H., Lian, D.Y., Khan, A., 2020b. Petrochemistry of high-Cr and high-Al chromitites occurrences of Dargai complex along Indus Suture Zone, Northern Pakistan. Episodes 43, 689–709.
Uysal, I., Tarkian, M., Sadiklar, M.B., Zaccarini, F., Meisel, T., Garuti, G., Heidrich, S., 2009. Petrology of Al- and Cr-rich ophiolitic chromitites from the Muğla, SW Turkey: implications from composition of chromite, solid inclusions of platinum-group mineral, silicate, and base-metal mineral, and Os-isotope geochemistry. Contrib. Mineral. Petrol. 158, 659–674.
Uysal, I., Ersoy, E.Y., Karslī, O., Dilek, Y., Sadīklar, M.B., Ottley, C.J., Tiepolo, M., Meisel, T., 2012. Coexistence of abyssal and ultra-depleted SSZ type mantle peridotites in a Neo-Tethyan Ophiolite in SW Turkey: constraints from mineral composition, whole-rock geochemistry (major-trace-REE-PGE), and Re-Os isotope systematics. Lithos 132–133, 50–69.
Uysal, I., Akmaz, R.M., Kapsiotis, A., Demir, Y., Saka, S., Avci, E., Müller, D., 2015. Genesis and geodynamic significance of chromitites from the Orhaneli and Harmancik ophiolites (Bursa, NW Turkey) as evidenced by mineralogical and compositional data. Ore Geol. Rev. 65, 26–41.
Walker, R.J., Carlson, R.W., Shirey, S.B., Boyd, F.R., 1989. Os, Sr, Nd, and Pb isotope systematics of southern African peridotite xenoliths: Implications for the chemical evolution of subcontinental mantle. Geochim. Cosmochim. Acta 53, 1583–1595.
Wu, W., Yang, J., Dilek, Y., Milushi, I., Lian, D., 2018. Multiple episodes of melting, depletion, and enrichment of the Tethyan mantle: petrogenesis of the peridotites and

chromitites in the Jurassic Skenderbeu massif, Mirdita ophiolite, Albania. Lithosphere 10, 54–78.
Xiong, F., Yang, J., Robinson, P.T., Xu, X., Liu, Z., Li, Y., Li, J., Chen, S., 2015. Origin of podiform chromitite, a new model based on the Luobusa ophiolite, Tibet. Gondwana Res. 27, 525–542.
Xiong, F., Yang, J., Robinson, P.T., Dilek, Y., Milushi, I., Xiangzhen, X.U., Zhou, W., Zhang, Z., Rong, H., 2017. Diamonds discovered from high–Cr podiform chromitites of Bulqiza, Eastern Mirdita Ophiolite, Albania. Acta Geol. Sin. (Engl. Ed.) 91, 455–468.
Zhou, M.F., Sun, M., Keays, R.R., Kerrich, R.W., 1998. Controls on platinum-group elemental distributions of podiform chromitites: a case study of high-Cr and high-Al chromitites from Chinese orogenic belts. Geochim. Cosmochim. Acta 62, 677–688.
Zhou, M.F., Robinson, P.T., Malpas, J., Edwards, S.J., Qi, L., 2005. REE and PGE geochemical constraints on the formation of dunites in the Luobusa ophiolite, Southern Tibet. J. Petrol. 46, 615–639.